UNIVERSITY OF BIRMINGHAM

Combining multi-modal non-destructive techniques to investigate ageing and orientation effects in automotive Li-ion pouch cells

fordham, arthur ; milojevic, zoran; Giles, Emily; du, wenjia; owen, rhodri; michalik, stefan; chater, philip; das, prodip; Attidekou, Pierrot ; lambert, simon; Allan, Phoebe; Slater, Peter; Anderson, Paul; jervis, rhodri; shearing, paul; brett, dan

Link to publication on Research at Birmingham portal

Combining multi-modal non-destructive techniques to investigate ageing and orientation effects in automotive Li-ion pouch cells

Arthur Fordham[1,2], Zoran Milojevic[2,3], Emily Giles[2,4], Wenjia Du[1,2], Rhodri E. Owen[1,2], Stefan Michalik[5], Philip A. Chater[5], Prodip K. Das[2,3], Pierrot S. Attidekou[3], Simon M. Lambert[2,3], Phoebe K. Allan[2,4], Peter R. Slater[2,4], Paul A. Anderson[2,4], Rhodri Jervis[1,2], Paul R. Shearing[1,2] and Dan J. L. Brett[1,2*]

[1] Electrochemical Innovation Lab, Department of Chemical Engineering, University College London, London, UK, WC1E 7JE

[2]The Faraday Institution, Quad One, Harwell Science and Innovation Campus, Didcot, UK, OX11 0RA

[3] School of Engineering, Newcastle University, Newcastle upon Tyne, UK, NE1 7RU

[4] School of Chemistry, University of Birmingham, Birmingham, UK, B15 2TT

[5]Diamond Light Source Ltd., Harwell Science and Innovation Campus, Didcot, UK, OX11 0DE
*Corresponding author: d.brett@ucl.ac.uk

Abstract

As the electrification of the transport sector progresses, an abundance of lithium-ion batteries inside electric vehicles (EVs) will reach their end-of-life (EoL). The cells inside battery packs will age differently depending on multiple factors during their use. Currently, there is limited publicly available research on the degradation of the individual cells recovered from real-world EV usage. Once they have been recovered from the vehicle, large-format pouch cells are challenging to characterise, measure their internal structure and determine state-of-health (SoH). Here, large-format (261 × 216 × 7.91 mm) Nissan Leaf cells are harvested from an EV and four complementary non-destructive techniques are used to distinguish the ageing of cells arranged in varying orientations and locations within the pack. The measurement suite includes infrared thermography, ultrasonic mapping, X-ray computed tomography, and synchrotron X-ray diffraction, and represents a unique combination of characterisation techniques. We found that each of the non-destructive diagnostic techniques corroborated each other yet provide different complementary insights. The influence of orientation and location of the cells is significant, with the rotated/vertically aligned cells differing significantly from the flat/horizontally aligned cells in mode and degree of ageing. These insights provide new information on cell degradation that can help to influence pack design and illustrates how rapid and relatively inexpensive technology can provide sufficient information for practical assessment compared to costly synchrotron studies. Such an approach can inform decision support at EoL and more efficient battery production reducing the wastage of raw materials.

Keywords: Automotive Li-ion pouch cell; electric vehicle; ageing; infrared thermal imaging; ultrasound acoustic measurement; X-ray tomography; deep learning; synchrotron X-ray diffraction.

1.   Introduction

The demand for lithium-ion batteries (LIBs) is increasing rapidly and will continue to do so for decades to come to supply the growing requirement in modern society. As well as increasing the rate of production, it is crucial to improve LIBs by enhancing power and energy density and extend the operating cycling lifetime in first-life applications. Currently, electric vehicle (EV) manufacturers consider a battery module within a pack to be at end-of-life (EoL) if it reaches 80% state-of-health (SoH). However, this decision tends to be based on limited or no knowledge of the SoH of individual cells. The individual cells inside the modules will have varying usage, and thus SoH, depending on factors such as orientation, cooling system and the location of the cell. A lack of information with respect to these factors often leads to some cells inside the pack being classified as at EoL when they have not fallen to 80% capacity, causing wastage of raw materials, energy consumption and time with significant cost implications. This highlights the importance of diagnosing the defects of individual cells so that EV batteries can be reused in second-life applications and only recycled when EoL can be robustly determined.

Rapid diagnostic techniques are required for SoH optimisation both for determining the second-life use of cells and to provide pack designers with the relevant information to compare positions and degradation. These techniques need to be low-cost, non-invasive, non-destructive, and rapid as well as effectively offering real-time operando prediction of the state-of-charge (SoC) and SoH. These diagnostic approaches can work alongside electrochemical and crystallographic methods to understand internal changes and defects occurring within cells.

Infrared (IR) thermography is a contactless and non-destructive technique that detects emitted radiation in the infrared range of the electromagnetic spectrum. With known parameters e.g. surface emissivity, camera distance, reflected and atmospheric temperature, the temperature field of the measured object's surface can be determined with high spatial and temporal resolution. For pristine automotive pouch cells, the technique is mostly used for validation of electrochemical-thermal,[1,2] and electro-thermal[3,4] models with experimentally obtained LIB surface temperatures during cycling.

Different cell orientations and tab positions can result in a heterogeneous distribution of the SoC,[5] current densities and voltage, which can cause temperature gradients across the battery.[6,7] While battery performance is strongly linked to temperature,[8] temperature gradients will influence ageing mechanisms during long-term usage,[9] Battery ageing characterisation by IR thermography has been covered in several studies: Veth *et al.*[10] highlighted the possibility of ex-situ IR thermography characterisation of large-format pouch cells (high/low current cycled and calendar aged) that have been aged to different degrees. In-plane ageing non-uniformities, across the surface of the cell, and 'real' EoL detection in battery second-life application by temperature derivative map analysis are presented.[11] Robinson *et al.*[12] used IR thermography to detect internal defects (gas pockets formed during cell ageing) using 'lock-in'

thermography. The influence of different orientations on in-plane temperature derivative maps for pristine and EV life aged large-format pouch cells are presented in the previous work by Milojevic *et al.*[13] IR thermography is well suited to large-format pouch cell measurements because of the flat geometry and can be a useful tool for battery manufacturers to minimise expected thermal/ageing gradients in the battery design stage and for in-plane ageing characterisation.

Ultrasonic testing is an acoustic technique that involves an externally generated signal produced from a piezoelectric transducer in contact with a cell.[14] This signal is propagated through the material before being recorded either by the same transducer *via* the reflection of the signal in the material or another transducer attached to the opposite surface of the cell. The technique allows analysis of the internal structure of the system because acoustic wave propagation is affected by the condition of the battery material. For further details on ultrasound testing, the reader is directed to recently published reviews by Majasan *et al.*[14] and Popp *et al.*[15]

The initial application of ultrasound to batteries focussed on fixed-point testing, which cannot probe heterogeneity across an entire Li-ion cell. Robinson *et al.*[16] were the first to report spatially resolved mapping using ultrasonic time-of-flight (ToF) analysis at 36 positions in a mobile-phone battery to identify inhomogeneities throughout the cell. They were able to distinguish the depth of the defect as well as determining that changes in signal amplitude correlated to the degree-of-lithiation of the respective electrodes. It was found that the ToF of the signal decreased with an increased state-of-charge. Robinson *et al.* then produced 12 lab-made Li-ion cells with purpose-built defects[17] and used ToF mapping to identify their presence. The acoustic scans could locate the depth of defect within the cell, and this was confirmed using X-ray computed tomography (CT) scans.

Other examples of ultrasonic mapping have observed electrolyte wetting in Li-ion pouch cells.[18] It was found that ultrasonic images of fresh and aged cells with different cycling conditions exhibit very different ultrasonic transmittance. This means that it can be used to probe structural defects and failure mechanisms within cells, such as electrolyte drying. In Deng's arrangement, the ultrasonic pulse was transmitted from one transducer and received from another on either side of the cell (transmission mode). The sensor had a diameter of less than 1 mm that allowed relatively high-resolution mapping and was able to determine the state of electrolyte and/or gas within a cell. Gauthier *et al.*[19] used ultrasonic transmission mapping (UTM) to determine how the depth-of-discharge (DoD), C-rate and age affect capacity retention and impedance of pouch cells cycled for 20,000 hours. The results found that poor ultrasonic transmission arises when wetting of the electrolyte does not occur in the pore spaces in the electrodes.

Although the work of Deng *et al.* and Robinson *et al.* produced abundant information about the internal structure of batteries, ultrasound mapping has principally been performed on small format cells, with the exception of Xie *et al*'s recent work who used ultrasonic techniques for non-automotive large

format cells.[20] Therefore, the research in this paper is the first to demonstrates the value of acoustic mapping on large-format cells that have been aged in electric vehicles and the value of the technique for use in manufacturing and industry. Moreover, it is the first time that multiple cells from a pack and the influence of cell orientation have been examined for large-size pouch LIBs using ultrasound mapping.

Over the last decade, X-ray CT has been widely used to non-destructively characterise the 3D structure of electrochemical materials and energy storage devices across multiple length and time scales.[21,22] Lu *et al.* employed nano-CT (126 nm voxel size) to reveal the structural heterogeneities formed under high C-rate cycling.[22] The microstructural evolution of Si particles was captured by using the high-speed synchrotron micro-CT by Taiwo *et al.*[23], and the cracking propagation and fracturing were tracked in real-time during the early stages of lithiation. These investigations at the nanoscale and microscale (from particle to electrode level) have facilitated cell engineering such as the development of new electrodes by understanding the role of materials structure in electrode degradation. Additionally, the advantages of macro-CT include its higher power output and larger experimental chamber, allowing for bigger samples in industrial applications.[24,25] At the cell level, extensive work has been undertaken to image cylindrical-type Li-ion cells using X-ray CT[26-29] to determine deformation in electrode architecture and multimodal characterisation has been used to provide a comprehensive understanding of 18650 cell ageing.[28]

To date, macro-CT studies of pouch-type cells are very limited. Bond *et al.* observed electrolyte depletion as a function of SoC.[30] Du *et al.* showed that cycle-induced gas generation could be tracked in a Li-ion pouch cell (400 mAh) by mapping the thickness evolution in 4D.[31] Shateri and co-workers illustrated the effect of ageing temperature on macrostructure using 19 Ah Li-S prototype pouch cells.[32] However, there is a need to characterise Li-ion pouch cells with high energy (up to 30 Ah per cell) and large size (up to hundreds of mm) dissembled from used EV modules to help determine the most appropriate forward-processing and use (i.e., reuse, recycling, recovery or disposal).[33] This requirement is based on the following: 1) Lack of information in the open literature. 2) Scanning pouch cells is more challenging than cylindrical cells because of the high aspect ratio (the laterally extended pouches, whose sizes are much larger than the detector's effective field of view, leads to difficulty in imaging the whole projection dataset of inner structures because of inadequate X-ray transmission in the extended direction). 3) Pouch-type cells are a major battery format and enable a higher pack level energy density than cylindrical-type due to improved space utilisation. 4) The impending challenge of dealing with a huge number of spent battery packs by 2030. Fast macro-CT scans could play a crucial role in evaluating the SoH for the 2nd life application. 5) Different battery cell sizes and configurations can have different fault and degradation mechanisms.[26,34] 6) Studying cells disassembled from used EV battery pack requires multiple expertise including mechanical, electrical and electrochemical.

4

X-ray diffraction (XRD) gives information about the crystallographic structure and composition of a material. Compared to lab-based sources, synchrotron X-rays are of higher intensity, are of tuneable energy and beam size and produce higher resolution diffraction patterns with improved signal-to-noise ratios. This allows for rapid data collection, enabling *in-situ* processes to be studied, with high-energy incident beams able to pass through a range of sample environments. In battery research, *in-situ* and *operando* studies using specially designed cells have been performed to elucidate structural and compositional changes during cycling and to monitor solid electrolyte interphase (SEI) formation and the evolution of strain within electrodes.[35] Long-duration experiments, where X-ray diffraction data are collected periodically over the lifetime of the cell, have enabled the long-term degradation of battery materials to be studied.[36] One such study on long-duration degradation by Leach *et al.* collected XRD data across nine sites on a single-layer small-format NMC811/graphite pouch cell over 900 cycles.[5] They found that the SoC of the edges and corners of the pouch cell increased slower relative to the centre of the cell on charging and contained a greater proportion of a fatigued phase. The authors speculated that these spatial inhomogeneities may become more pronounced in larger format pouch cells or cylindrical cells.

Synchrotron X-ray diffraction has been used to map the spatial inhomogeneities within NMC622/Li pouch cells, with the technique termed High-Energy Lateral Mapping (HELM).[37] Mattei *et al.* tested two samples using HELM. They lab-assembled a seven-layer pouch cell in pristine condition and a single cathode layer taken from an equivalent cell that had been aged by CCCV cycles in the lab (as opposed to aged in real-world application) to 10% of its initial discharge capacity. In the pristine pouch cell two parameters were mapped, the loading level and unit cell volume of NMC622, and were both found to be homogeneous across the entire area of the cell. The only exception was a substantial excess of NMC622 present on the sample tab. The single-layer cathode sheet possessed a few 'hot-spots' where the cathode material was of higher SoC (inferred from the unit cell volume) and of a lower abundance. On closer inspection, a second NMC622 phase of higher SoC coexisted within these hotspots with a primary phase that had the same SoC as the rest of the cell. HELM (or High-Energy XRD (HEXRD)) has been used to spatially map Li plating, the extent of lithiation of the graphite anode and the cathode SoC in a single layer NMC532/graphite pouch cell.[38]

This paper explores the value of multi-modal, non-destructive diagnostic techniques, including thermal imaging, ultrasound mapping, X-ray computed tomography (CT), and synchrotron X-ray diffraction, to examine five large-format multi-layer Li-ion Nissan-Leaf cells that were positioned in different orientations and locations within a used vehicle battery pack. Applying these techniques to cells of this large size, which have been aged in real-world conditions, is a novel approach. These techniques demonstrate differences in the homogeneity of ageing across cells and the importance of cell orientation and location within the pack. Insights into future battery pack design by demonstrating which cell

orientations will optimize performance and minimize degradation across all cells can be drawn from the study, as well as improvements to recycling strategies for EoL cells.

2.   Experimental

2.1   Battery Specification

Experiments were carried out on automotive large-format pouch cells (blended cathode consisting of lithium manganese oxide (LMO) with lithium nickel-cobalt-aluminium oxide (NCA), and graphite anode) extracted from two first-generation Nissan Leaf battery modules.[39] These pouch cells have a capacity of 32 Ah, dimensions of ($261 \times 216 \times 7.91$ mm) and consist of 17 double-sided cathode sheets and 18 double-sided anode sheets. The battery pack contains 48 passive cooled modules (Figure 1a) arranged in two side stacks (2×12 modules) and one rear stack (1×24 modules). Before the modules were removed from the EV, battery management system statistics showed the battery pack's SoH to be 76.96 %, where SoH throughout the paper refers to capacity fade. For this study, two modules with different orientations in the battery pack (Figure 1a right) were disassembled to the cell level. In each module, four batteries (labelled 1-4 from the bottom of the module) are connected in 2P $\times$ 2S arrangement and to establish a connection with busbars, cell tabs were cut during manufacturing depending on the position in the module (Figure 1b). For analysis in this study, two middle cells (No. 2 and No. 3) from selected modules were tested and compared and their orientations in the pack are shown in Figure 1c (**F-for flat aged and R-for rotated aged modules**). For comparison to the aged cells, a pristine cell was also investigated in Sections 2.3 and 2.4. The Pristine cell was obtained from a second-generation Nissan Leaf battery with a cathode consisting of $LiNi_{0.5}Mn_{0.3}Co_{0.2}O_2$ (NMC532). The dimensions were the same as first-generation cells. Whilst the chemistry differs from the first-generation aged cells, it is expected that the lack of degradation will be evident and therefore provide a suitable comparison. Each cell was discharged to 3 V for all measurements unless otherwise stated.
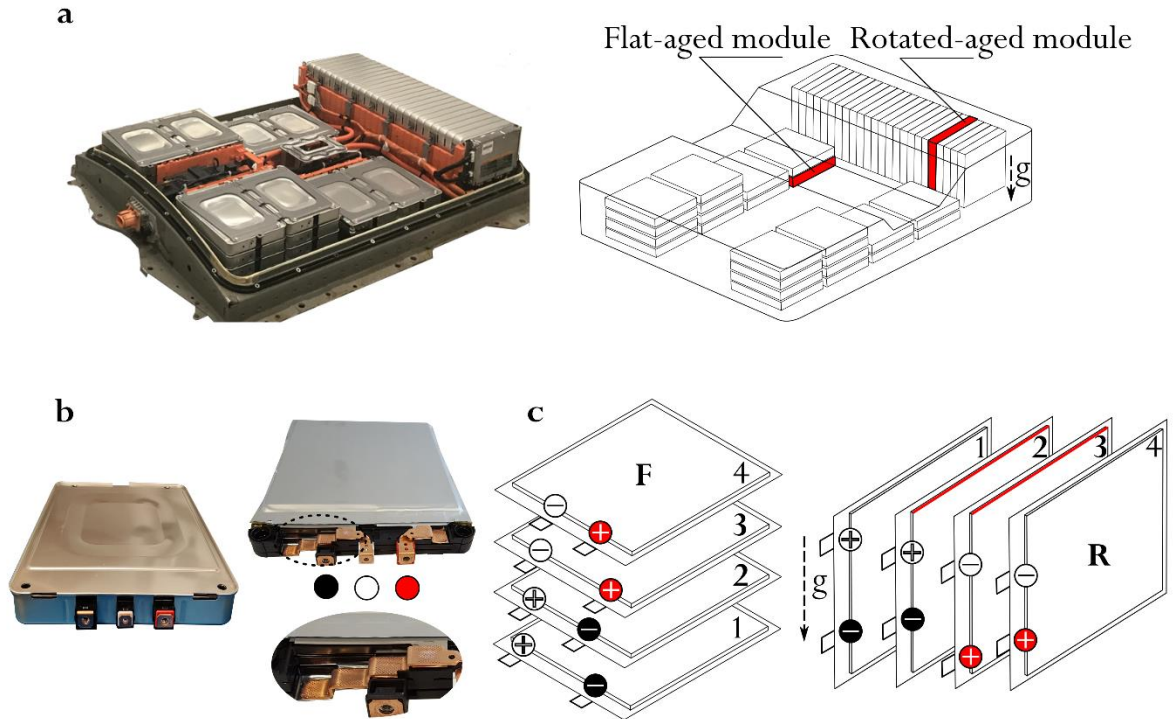
Figure 1. a) Battery pack and position of tested modules in the pack. b) Module with casing (left), without casing and busbar-tabs connections in the module and gravity vector direction (right). c) Positions of the tested cells (2,3) in the module and their orientations in the pack (F-for flat and R-for rotated aged), for rotated aged cells edges opposite to the gravity vector are marked with the red lines.

2.2   *Thermal imaging measurement procedure*

Thermal imaging measurements were conducted with a FLIR A655 thermal camera, which was calibrated for temperature range (–40 ℃ to 150 ℃) with 640 × 480 pixel resolution at 1 Hz frame rate. Thermal sensitivity for the camera is less than 30 mK with a maximal error of ±2%. The surface of the cell was painted with Tetanal Camera Varnish Spray/Black paint, with a measured emissivity value of 0.96 to eliminate reflections. During measurement, the cell was placed in a bespoke holder made from POM-C acetal solid plastic material. Aluminium plates were used to ensure a good connection between lead wires and the tabs (see Figure S1). Batteries were charged with a constant current (CC) of 50 A (*ca.* 1.5 C compared to nominal capacity) and after that held at 4.2 V constant voltage (CV) until the current dropped to less than C/20 and then left to rest for 1 hour. After that, batteries were discharged at 50 A CC until the voltage reached 2.7 V (see Figure 2a). Cell cycling was performed using a BioLogic HCP-1005 potentiostat.

During discharging, cell surface temperature and capacity were measured within the environmental chamber (Binder GmbH), set to 25 °C. The chamber was switched off 10 min before the end of the rest period (Fan off in Figure 2a) and during thermography measurements, to enable unified cell cooling conditions.

2.3   Ultrasonic mapping measurement procedure

Ultrasound mapping experiments were undertaken on the four Li-ion Nissan Leaf pouch cells used in the thermal imaging measurements as well as a pristine Nissan Leaf pouch cell, which was yet to be used inside a battery pack. The Pristine cell was measured as a reference to compare with the two aged flat cells (F2 and F3) and the two aged, rotated cells (R2 and R3).

The ultrasonic mapping measurements (Figure S2) were performed using an Olympus Focus PX phased-array instrument (Olympus Corp., Japan) with a 5 MHz 1D linear phased array probe consisting of 64 transducers. The transducer had an active aperture of 64 mm with an element pitch (centre-to-centre distance between elements) of 1 mm. The cell was covered with ultrasonic couplant (Fannin UK Ltd.), prior to every scan to ensure good acoustic transmission. The transducer was moved along the length of each cell at a fixed pressure using an Olympus GLIDER 2-axis encoded scanner with the step size set at 1 mm to give a resolution of *ca.* 1 mm^2. Due to the large size of the cells, the active aperture of the probe was wide enough to cover 1/3 the width, meaning that three measurements for each cell were taken and the data was combined to form the colour maps.

Data from the ultrasonic signals were analysed using FocusPC software. The waveforms recorded by the transducer were exported and plotted using custom Python code to compare how the signal changes at different points in the cell. For consistency, a specific ToF range was selected for all cells, chosen because it is where the part of the waveform, known as the 'echo-peak', is located.[40] The echo-peak is useful to monitor as it is where the waveform has travelled the whole way through the cell and reflected from the back surface, so characterising the entire cell. The maximum amplitude of the ultrasonic signal within this ToF range, at each point, are combined to produce a colour map. The signal amplitude is a proportion of 100 where 100 is the maximum intensity of the signal, meaning that the signal has been attenuated the least as it travels through the cell, and 0 is the minimum intensity. The intensity is absolute and not normalised across all scans, meaning that an amplitude values on different cells can be directly compared. The Pristine cell is a second-generation Nissan Leaf pouch, different to the first-generation aged cells of varying orientation. The authors were not able to acquire an identical first-generation pristine Nissan Leaf cell. Nonetheless, it was expected that the Pristine cell would contain a uniform internal structure regardless of the specific chemistry and this would be identified in an ultrasound map consisting of a single colour (or narrow colour range).

To better understand the results of the ultrasonic mapping, the areas with the highest acoustic attenuation (red area against the rest of the area in the colour map) were quantified in each sample. Initially, the RGB images (Figure S3a) were converted to 8-bit images using ImageJ.[41] The area of the entire large pouch (S_{All}) was measured (Figure S3b), and the Otsu thresholding[42] was then applied to label the red region ($S_{high-attenuation}$) by referencing the associated RGB image. Next, the connected pixels

were segmented as a class (Figure S3c) and measured as $S_{high-attenuation}$. Therefore, the fraction of the area with relatively high attenuation (η) can be calculated by using Equation (1).

$$\eta = \frac{S_{high-attenuation}}{S_{All}} \tag{1}$$

These results were quantified further by using the same image processing method to divide each ultrasonic map into nine sub-sections as displayed in Figure S4. For each sub-section, the percentage of highest acoustic attenuation (red-region) was calculated. The calculations allowed the spatial distribution of the highly attenuating areas to be better understood.

2.4   X-ray computed tomography and image processing

Both rotated (R2) and flat (F3) pouch samples were scanned using a lab-based X-ray CT instrument (Nikon XT 225, Nikon Metrology, UK) after the acoustic measurements. Here, corner scanning was chosen due to the large sample size (261 × 216 × 7.91 mm), high aspect ratio (length against thickness is *ca*. 33) and high density of the materials (LMO and NCA). Thus, each cell was tilted 45 degrees and placed on a large plastic holder fabricated using a 3D printer (Ultimaker S3, UK). The experimental setup is displayed in Figure S5. The voltage and beam current were set at 200 kV and 150 µA, resulting in a power of 30 W. A cone-beam employing a tungsten target was used with an exposure time of 1 s per projection, and a total of 3185 projections were collected per tomogram with a 0.5 mm Sn filter. The 2028 × 2028 pixels CCD camera detector achieved a voxel resolution of 45 μm with a field-of-view of ca. 91 × 91 mm^2.

The raw X-ray projections were automatically reconstructed using Nikon CT Pro 3D software (Version XT 4.4.4, Nikon Metrology, Tring, UK) employing a cone-beam filtered back projection algorithm. All samples were scanned under identical conditions. The reconstructed 16-bit greyscale TIFF image sequences were initially cropped to remove the exterior border and highlight the region of interest (ROI, approximately 60 × 30 × 7 mm) before importing into Dragonfly (ORS, Montreal, Canada) for subsequent image processing. The Gabor filter[43] was applied to improve the contrast of raw images before further segmentation and final 3D visualization (Avizo 2019.4, Thermo-Fisher Scientific, USA). The deep learning (U-Net) algorithm[44] was used to train a 3D model to identify and classify the electrodes plus current collectors (green), electrolyte (pink), gas or electrolyte depletion (yellow) and exterior air (blue) based on the greyscale, object shape and orientation. Six ground-truth frames at multiple local regions were manually segmented to train the 3D model. Hence, four phases of U-Net computational segmentation are shown in Figure S6. The profile of the training procedure, including the epochs against the loss function, is also presented in Figure S6. The trained model was then used to automatically segment the entire ROI volume. Afterwards, quantification was performed to obtain the volume of electrolyte depletion and the associated 3D thickness map. More details of the thickness measurement approach can be found in Du *et al*.[31]

2.5 Synchrotron XRD measurement procedure

Powder X-ray diffraction data were collected on three of the Nissan Leaf pouch cells on beamline I12-JEEP[45] at Diamond Light Source. These were two pouch cells that had been flat-aged (F2 and F3) and one that had been rotated-aged (R3) within the battery pack. Each cell was measured one at a time in a customised holder (Figure S7), with the cell secured between two PEEK (polyetheretherketone) clamps at the top and bottom. These synchrotron measurements were all undertaken when the cells were at the bottom of discharge (~ 0% SoC). A beam energy of 67.98 keV ($\lambda = 0.1824$ Å) and beam size of 0.5 mm by 0.5 mm were used with a sample-detector distance of 1055.5 mm, calibrated using a LaB_6 standard. Each cell was translated in 5 mm steps both horizontally and vertically in a raster scan starting from the top-left corner of the cell and finishing in the bottom-right corner. X-ray diffraction data were collected at each point with an exposure time of 5 s. Diffraction rings were imaged on a 2D Pilatus 2M CdTe detector with a 172 µm × 172 µm pixel size and dimensions of 1475 × 1679 pixels and integrated into 1D diffraction patterns using DAWN.[46] The number of points scanned by the high energy synchrotron X-ray radiation allowed HELM across the entirety of each cell to be produced.

Rietveld refinement was performed on all of the individual diffraction patterns using the same input file (created in jEdit[47] version 5.5) with the software TOPAS version 6.[48] Diffraction peaks were observed for six phases, the aluminium and copper current collectors, the two cathode materials, $LiMn_2O_4$ and a layered oxide (refined as $LiNi_{0.8}Co_{0.15}Al_{0.05}O_2$ or NCA), graphite from the anode and polypropylene from the laminate pouch cell casing. For all refinements, Cu was used as an internal standard of fixed lattice parameter ($a = 3.61505$ Å)[49] and a sample to detector distance offset function was refined so that variations in sample thickness and sample-detector distance could be accounted for. Diffraction patterns from each cell were refined in batches with the values of variables exported in tabulated form. These were cross-referenced with the motor positions and the spatial variation of each parameter was plotted using MATLAB to produce a HELM plot for each cell.

3. Results

3.2 IR Thermal measurements

Thermal imaging was performed during the discharge step of cell cycling and the results are presented in two sections. The first section covers obtained lumped parameters results (capacities and mean temperatures relative to the initial cell temperature (T_{Mean})), whilst the second section covers the spatial thermal behaviour of the cells.

3.2.1 Lumped parameters

An example of the test procedure used for each of these tests and a typical voltage profile is shown in Figure 2a. Figure 2b depicts the voltage versus capacity graphs obtained during the thermal imaging

discharging cycle for the four batteries investigated. Mean relative temperature profiles during discharging for all batteries are shown in Figure 2c. Measured cell capacities (Q) and mean relative temperatures (T_{Mean}) at the end of discharge are displayed in Table 1.
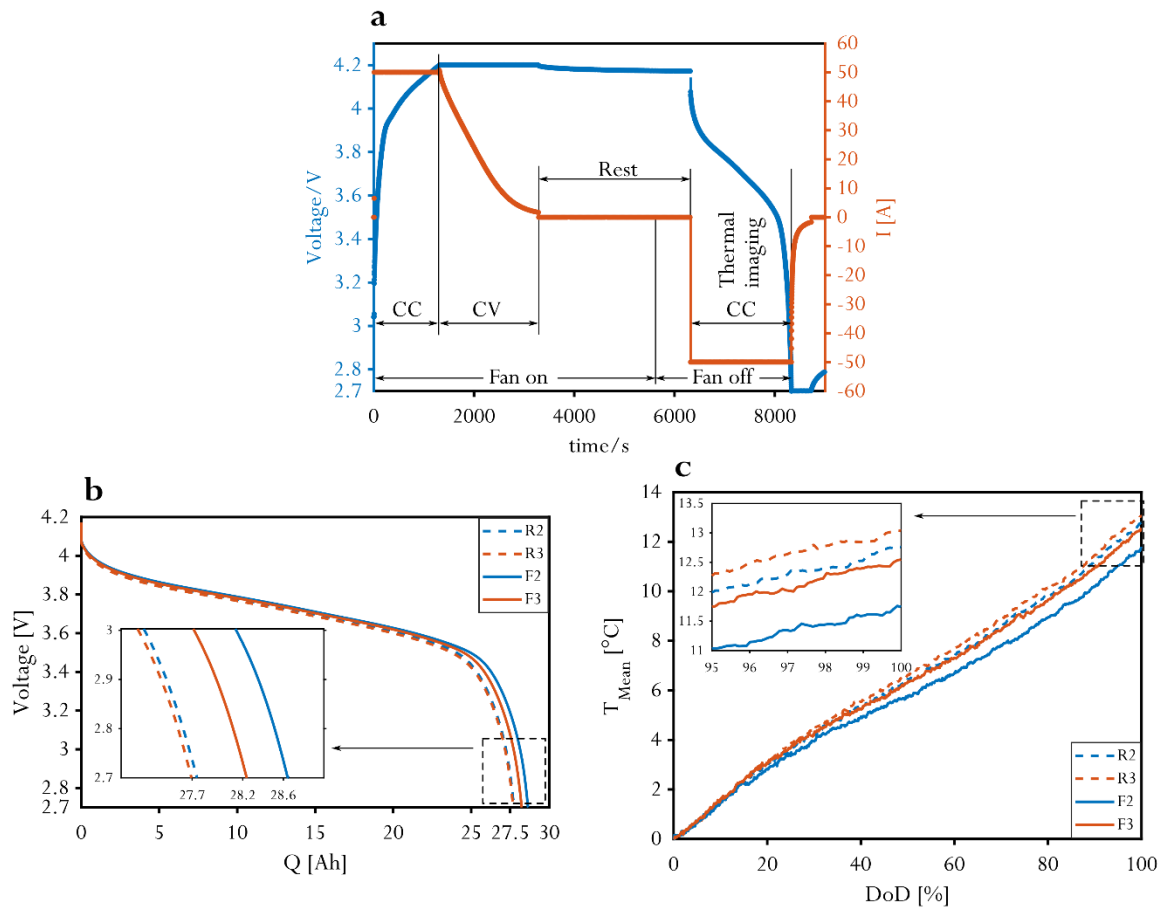

Figure 2. a) Thermal imaging cycling procedure–- constant current charging (CC) at 50 A, 4.2 V constant voltage (CV) until the current dropped to less than C/20 followed by a 1-hour rest period. Thermal imaging was performed during CC discharge at 50 A until the voltage reached 2.7 V with the environmental chamber turned off; b) voltage versus capacity measured during thermal imaging discharging cycle; c) mean relative temperatures T_{Mean} recorded during thermal imaging.

Table 1. Measured capacity (Q) and mean relative (T_{Mean}) temperatures at the end of discharge for the tested cells.

	New	F2	F3	R2	R3
Q [Ah]	32.5	28.6	28.2	27.8	27.7
SoH [%]	100	88.0	86.8	85.5	85.2
T_{Mean} [°C]	-	11.7	12.5	12.8	13.0

From Table 1, higher capacities are measured for flat-aged batteries (F2 and F3, 28.6 Ah and 28.2 Ah, respectively) while lower capacities are measured for rotated-aged batteries (R2 and R3, 27.8 Ah and 27.7 Ah, respectively). The maximum capacity-based SoH difference is 2.8 %. T_{Mean} at the end of discharge is in good correlation with the measured capacities, where batteries with lower capacities reached higher temperatures compared to batteries with higher measured capacities.

3.2.2   Spatial variation of temperature

While previously presented average results show that rotated-aged batteries have lower capacities and higher temperatures at the end of discharge (see Table 1) the temperature maps were further processed in two ways to investigate the spatial ageing difference between flat- and rotated-aged batteries. Firstly, the position of the maximum relative temperature (T_{RelMax}) over the course of discharge was tracked and extracted at every second in the depth of discharge range to generate the hot-spot map shown in Figure 3a; here the depth of discharge (DoD) of each point is indicated using a colour scale. Secondly, the position of the maximum temperature derivative (dT/dt) was calculated and tracked over the course of discharge to generate the hot spot map shown in Figure 3b, again the DoD is indicated using the colour scale. The dT/dt measurements give an indication of where the biggest temperature changes are occurring each second. The T_{RelMax} provides an indication of where the majority of the heat generating activity has been occurring whereas the dT/dt measurements gives information about where the largest changes in heat generating activity is occurring at that point in time regardless of whether it is the highest temperature across the surface of the cell at that point. Both sets of results are also shown in Video S1.
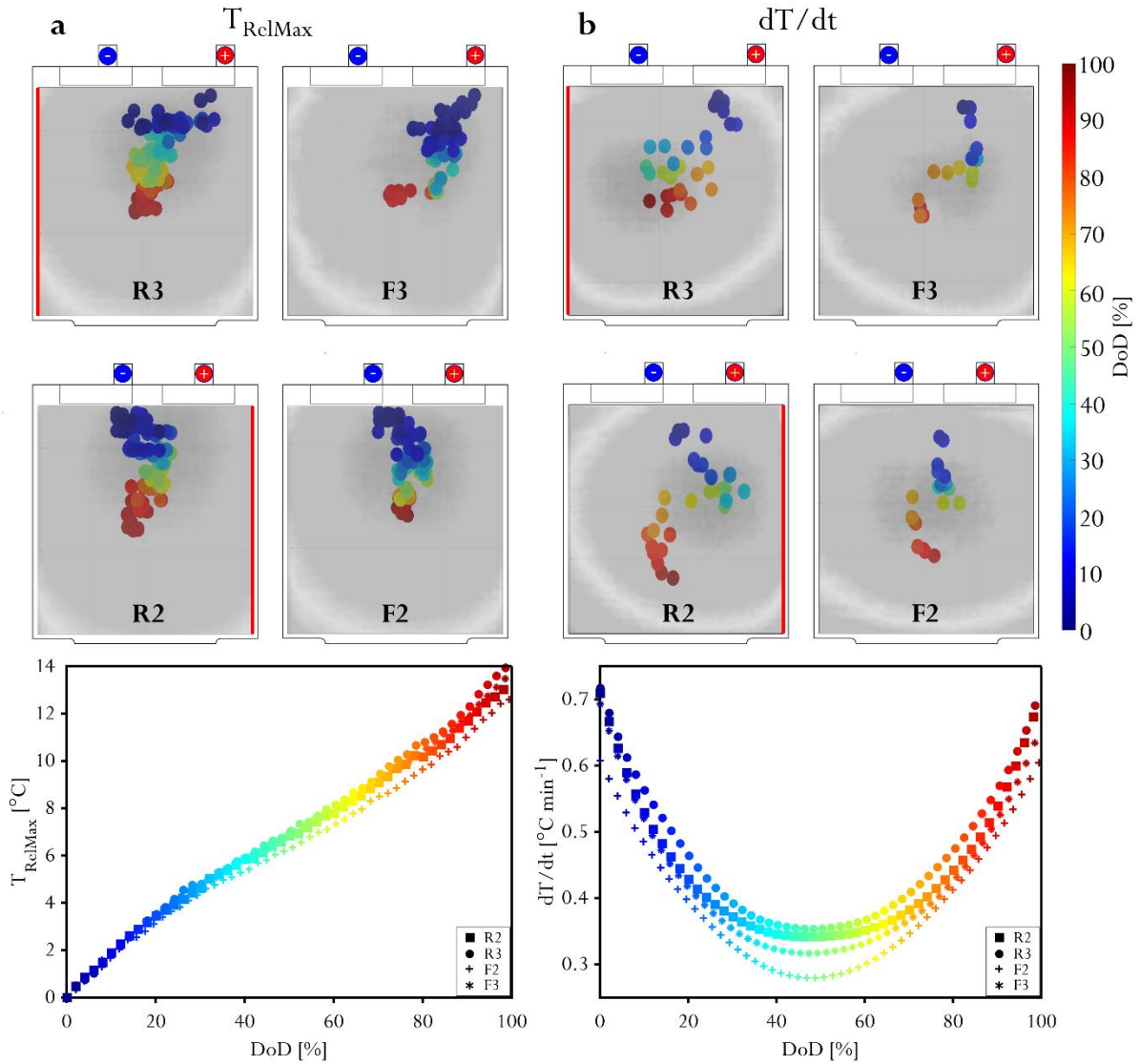
Figure 3. a) Hot-spot maps showing the changing position of T_{RelMax} over the course of discharge for each of the four cells. b) Hot-spot maps showing the changing position of the maximum *dT/dt* during the course of discharge. Depth of discharge for each of the points is shown in using the colour scale. Plots showing how T_{RelMax} and maximum *dT/dt* are shown below the images. Maps (in grey) over the surfaces present T_{Rel} (a) and *dT/dt* (b) at 40 % depth-of-discharge. For rotated cells, the edges oriented upwards are marked with red lines to illustrate the effect of gravity. The gravity vector is displayed in Figure 1c.

Figure 3 indicates that hot-spot positions extracted from T_{Rel} maps (Figure 3a top) are influenced by the geometry of the tabs, especially at the beginning of discharge (at low DoD). At low DoD, hot-spot positions are closer to the positive tab for cells F3 and R3, while for F2 and R2, they are closer to the negative tab. For the rotated cells, this position is closest to the edge oriented downwards. As DoD increases, the position of the hot-spots shifts towards the centre of the cell for all cells. The T_{RelMax} hot-

13

spot position can be associated to the area of the cell undergoing most electrochemical activity and resistance, causing a higher temperature. For all cells, the T_{RelMax} hot-spot never drops below the centre of the cell throughout the whole discharge, implying that cell usage is greatest near the respective tabs at the start of DoD and then shifts to the centre at high DoD. R3 and F3 cells reached slightly higher T_{RelMax} values at the end-of-discharge compared to R2 and F2 (Figure 3a bottom).

Hot-spot positions extracted from dT/dt maps show different behaviour. Values of the hot-spots (dT/dt_{Max} in Figure 3b bottom) for rotated aged cells (R2 and R3) are higher compared to the flat-aged cells (F2 and F3). This increased temperature suggests that rotated cells underwent greater stress and resistance during discharge compared to the flat ones, leading to greater ageing after long term cycling. These results are in good correlation with measured capacities presented in Table 1. The hot-spot positions extracted from dT/dt maps (Figure 3b top) provide more interesting results. At the beginning-of-discharge (<20% DoD), dT/dt_{Max} hot-spot positions are similar and are aligned between the tabs. This result differs compared to T_{RelMax} positions (Figure 3a top) at the same low DoD. As DoD increases, the flat-aged cells (F2 and F3) dT/dt_{Max} hot-spots shift in a similar direction toward the centre. In contrast, the rotated-aged cells (R2 and R3) hot-spot shift is less uniform. Between 20-60% DoD, there is movement of hot-spot position to the side of the cell that was oriented upwards, as illustrated in (Figure 1c). For R2, this direction was to the positive tab and for R3 it was to the negative tab. From 80-100% DoD, the hot-spot position shifts towards the centre. For R2, there is greatest dT/dt_{Max} shift toward the bottom of the cell, which is not seen in R3 or the flat cells.

3.3   Ultrasound measurements

The ultrasonic mapping results are dependent on the amplitude and ToF of the signal as it passes through the battery material. The amplitude of the signal is affected by the medium through which it passes. The wave will be attenuated by changes in the internal structure of the cell. As the cell ages, changes occur within the layers of the cell structure, the electrolyte distribution and gas that is generated. An ultrasonic signal passing through wetted electrolyte is attenuated far less than travelling through an 'unwetted' section where the electrolyte has been consumed and dried up. For a 'dry' electrode, the ultrasonic signal can only transmit between particles inside the internal structure. These particles are at different orientations and shapes causing reflection and scattering, leaving the acoustic signal greatly attenuated. However, for the wetted areas, the electrolyte acts as a medium for the ultrasonic signal to transmit, allowing the wave to propagate with minimal attenuation.

The amplitude and ToF of the ultrasonic' signal will also be affected by changes to the internal structure induced by cycling and ageing. The speed of the ultrasonic wave, c, through the cell is related to Young's modulus, E, and density, ρ (see Equations (2) and (3)):

$$c = \sqrt{\frac{E}{\rho}} \qquad (2)$$

$$ToF = \frac{L}{c} = \frac{L}{\sqrt{\frac{E}{\rho}}} \qquad (3)$$

ToF thus increases with the distance the signal travels, *L,* and with increasing density, and decreases with growing elastic moduli. The signal travels faster through a medium with greater elastic modulus.

Figure 4 displays the results of the ultrasound mapping measurements for each cell. Colourmaps for each cell are shown with the red end of the spectrum representing higher signal attenuation (lower amplitude) and the green end indicating a more intense signal (higher amplitude). The amplitude is not normalised across all scans, meaning that colours on different cells can be directly compared A waveform plot indicating how the signal changes across the surface of the cell is included above each colourmap. Maps are generated based on the amplitude of the signal in the chosen gate, over a ToF range of 26-38 µs, this region was chosen because it contains the 'first echo' peak. A 'first echo' peak is generated by the signal that has travelled through the whole cell, before being reflected. This signal is analysed since it gives information about the entire internal structure of the cell.
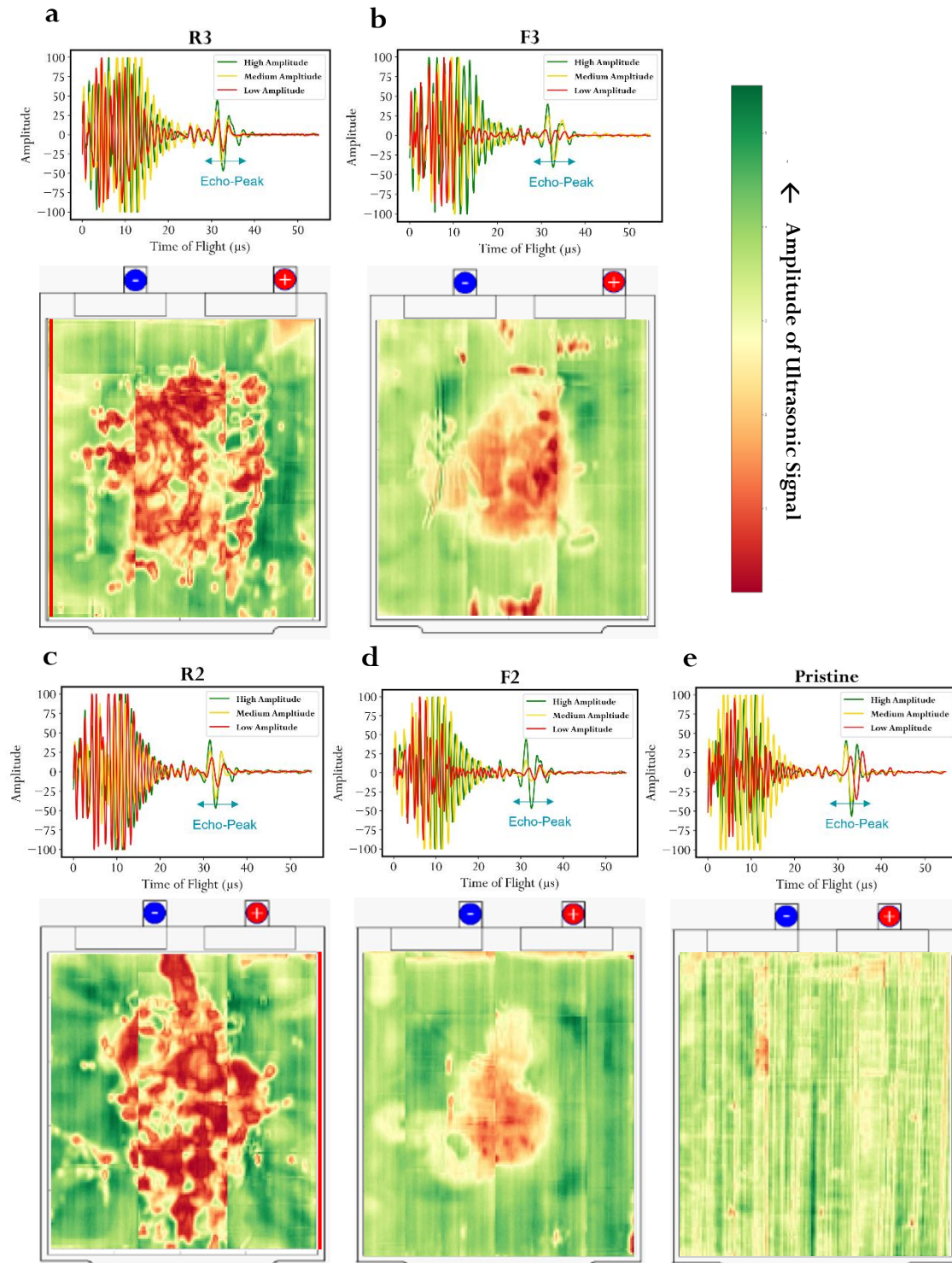
Figure 4. Ultrasonic colour maps and corresponding waveforms for each cell. The waveform plot displays three separate signals overlayed for different parts of the cell. The green line indicates an area of high signal amplitude, indicating it has been attenuated least. The red line indicates an area where the signal has been most attenuated and hence has the smallest amplitude, whereas the yellow waveform is in an area where the signal is dampened an amount in between the two. The colour maps represent the amplitude in the chosen gate (Blue Arrow) across every point in the cell. **a**) R3 and **c**) R2 are cells of rotated orientation inside the battery pack. **e**) Pristine, is a cell

before it has been cycled inside a pack **b)** F3 **d)** F2 are cells of Flat orientation inside the battery pack. For rotated cells, the edges oriented upwards are marked with thicker red straight lines to illustrate the effect of gravity.

Examining the flat (F2, F3) cells, the darker red and yellow areas are present in a central uniform position, indicating low amplitude signals. F3 has more areas where the signal has been attenuated relative to F2, but both occur in similar positions. The edges have very few red areas implying that the signal has passed through at high amplitude. In contrast, rotated cells (R2, R3) have far more areas of high attenuation, spread in a non-uniform position across the whole cell. For R3, the positive tab was oriented lowest, relative to the bottom of the battery pack, and the low amplitude signal appears to be seen across both sides of the cell. For R2, the negative tab was oriented lowest, and the red, low amplitude area stretched across the whole middle of the cell and towards the positive tab. The different patterns seen in the colour maps appear to be dependent on cell orientation. An image processing method, outlined in Section 2.3, was used to spatially quantify the distribution of the acoustic attenuation in nine sub-sections of each cell. These images are displayed in Figure S4. The results found that the sub-sections with highest percentages of acoustic attenuation in the rotated cells, particularly the sub-sections closest to the upwards edge. This phenomenon was most notable for R2, which had a 32% area of high attenuation on the upwards edge compared to 24% in the sub-section containing the edge oriented downwards. For reference, a pristine second-generation Nissan Leaf pouch cell was also scanned using ultrasound ToF measurements. Although this cell is of a different chemistry, the new, non-aged nature of the cell is expected to be representative of a fresh first-generation Nissan Leaf cell that has not been subjected to uneven stresses resulting in degradation. In the centre, there is no area of low amplitude signal as in the aged cells, with a uniform acoustic signal generated across the surface of the cell. Relative to the aged cells, the waveform plot for the Pristine cell displayed the highest amplitude intensity of signal, within the echo-peak range.

The same image processing method was also used to quantify the overall fraction of the most degraded areas across each cell. As seen in Table 2, the Pristine cell, expected to have a completely uniform structure before cycling, displayed a fraction of differing colour of 0.58%, confirming the hypothesis. The rotated cells, R2 and R3, contained a far greater fraction of degradation than the flat cells, F2 and F3. The similar fraction of ~25% for each of the rotated cells confirms the consistent negative effect of this orientation on SoH and correlates to the similar SoH values seen in Table 2. The flat cells show a fraction that is far less than the rotated cells with F2 less than F3. SoH and capacity of F2 is recorded as slightly higher than F3, which matches the results seen in the image processing of the ultrasound data, further emphasising the success of acoustic techniques as a quantitative diagnostic method.

17

Table 2 – Percentage areas of high acoustic attenuation in each cell calculated using image processing.

	Pristine	F2	F3	R2	R3
Percentage area of high acoustic attenuation [%]	0.58	6.36	12.6	24.3	21.5

3.4   X-ray CT measurements

The acoustic technique is regarded as a low-cost and rapid probe to identify the initial gas distribution and other defects within a pouch cell.[40] The previous section showed that Li-ion cells, operated in different orientations inside the pack, displayed distinct variations in their associated acoustic maps, thought to be associated with areas of internal cell degradation. Macro-CT scans were performed on the representative samples at the corner opposite the tabs; namely Pristine, rotated-aged (R2) and flat-aged (F3) samples. A lab-based CT scanner, with a spatial resolution of 45 μm pixel size, was employed to complete and validate the prior acoustic results by providing architecture information in 3D at the 'cell level'. To better observe and quantify the multi-class features in each sample, the trained U-net 3D model was applied to segment these 16-bit greyscale images, and the results (Figures 5 & 6) demonstrate the deep learning-assisted segmentation tool has a valuable role in battery analysis by X-ray imaging.

In Figure 5, 2D longitudinal slices, taken from the corners (Figure S5), of three large Li-ion pouch cells are presented. Although the nature of geometric limitation (high-aspect ratio) restricts further high-resolution acquisitions, it is sufficient to obtain the typical parallel layer structures. Higher density materials will have a brighter phase in the X-ray image because of high X-ray attenuation, and vice versa. In these side views at the X-Z plane, the electrodes (both anode and cathodes), electrolyte, separators and some defects were resolved based on their density.

Figure 5a demonstrates the non-defects in the end cell. It is important to note that the Pristine Nissan-Leaf cell is a second-generation design containing more structural layers than the other first-generation aged cells analysed, and a different chemistry.[50] Nonetheless, the X-ray CT result confirms that the electrode layers are better aligned, and the electrolyte is fully wetted. The R2 cell (Figures 5b&c) has the most prominent electrode misalignment compared to F2 and Pristine cells. This observation is confirmed by drawing a red dashed line perpendicular to the electrode layers, showing that the misaligned distance is ~4 mm. Misalignment is a problem because it causes a reduction in surface area overlap between the electrode layers, meaning that lithium is left inactive during cycling and in turn causes capacity loss.[5]

More importantly, Figures 5b–e show that gas formation related to electrolyte depletion was observed in both R2 and F3 samples after ageing. X-ray imaging and subsequent quantification of liquid electrolyte in this region allow for comparison of electrolyte 'depletion' that can result from different

18

displacements. The arrows identify black regions (low X-ray attenuation regions) where the electrolyte was partially decomposed generating 'pocket-like' gas products (i.e., CH_4, CO and CO_2, etc) between the electrodes after long-term use. R2 has a larger area of electrolyte depletion than that in F3, and the confirmation of such phenomena becomes more obvious in the 2D front view (shown later in Figures 6b & e). Whilst these scans only cover the corner of the cells, the gas evolution in the pocket of cell indicates that there has been electrode depletion throughout the centre of the cells, as displayed in the ultrasonic mapping measurements.

In Figures 5c & e, the segmentation of each cell is displayed. Using conventional segmentation approaches, such as thresholding and Otsu methods,[42] it is almost impossible to differentiate the region of electrolyte depletion (marked by yellow) from the region of outside area (marked by blue). This arises because these two regions have similar X-ray attenuation (similar greyscale values), and therefore the black regions will be classified as the same type. Therefore, to distinguish these regions, a four-phase segmentation model was trained, as shown in Figure S6a; the training was completed after 43 epochs, according to the loss function (Figure S6b). The four phases are then automatically labelled in colours (blue: outside, green: electrodes and separators, pink: electrolyte, yellow: electrolyte depletion). Whilst the electrode layers can be clearly identified by visual inspection, they have not been segmented separately in this study.
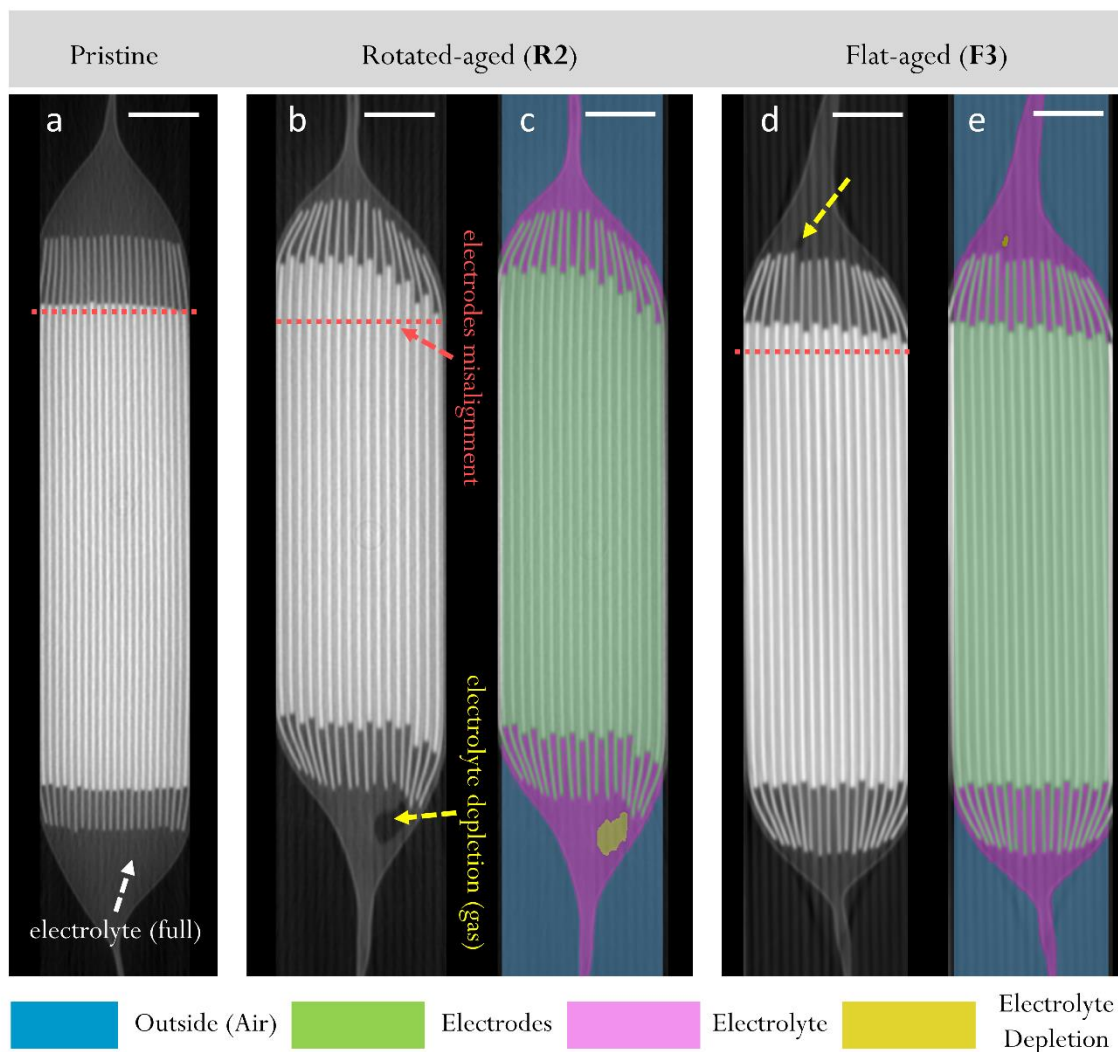
Figure 5. Tomographic slices of large Li-ion pouch cells at the corner opposite the tabs under the status of (a) pristine, (b & c) rotated-aged, and (d & e) flat-aged, showing the overall macrostructure under the two different placements. The side views (X-Z plane) are extracted from the ROI volumes. The pink arrows highlight the low X-ray attenuation zones (black area since almost no loss of X-ray photons), indicating the electrolyte loss after ageing, in particular for the rotated-aged (R2) sample. The red dashed lines are drawn to indicate the alignment of the electrode layers, suggesting the R2 sample has the highest misalignments among all samples. The trained U-net model was applied to the greyscale images (b & d), demonstrating deep learning-assisted segmentation (d & e) of three labelled phases (blue: outside, green: electrodes and separators, pink: electrolyte, yellow: electrolyte depletion). The scale bars represent 4 mm for all figures.

Similarly, 2D cross-sectional slices (front views) and their associated label images are demonstrated in Figure 6. Again, no defects are visible at the edge of the Pristine sample (Figure 6a). However, large-scale gas channels up to 6 mm can be observed in the R2 sample, as shown in Figure 6b & c. This also demonstrates the importance of X-ray CT compared with other destructive methods which are unable to observe the location of the gas products. A smaller gas pocket with a length of up to 2 mm was found (Figures 6e & f) in the F3 sample. This image selected from the front view corroborates prior observations from the side view.

As electrolyte depletion leads to gas generation, it is crucial to quantify the volume produced in order to understand the state-of-health (SoH) for such a large-size, high-capacity Li-ion pouch (up to 32.5 Ah). The gas volumes *via* electrolyte decomposition for R2 and F3 samples are rendered in 3D, as shown in Figures 6d & g, respectively. Here, the 3D volume of electrolyte depletion is presented, and other phases are deliberately removed. Figures 6d & g illustrate that both R2 and F3 have the 'rod-like' or 'strip-like' gas feature. The thickness distribution of gas for the R2 cell ranges from 100 to 1100 µm, whilst the F3 cell has the smaller values (from 100 to 710 µm) as shown in Figure 6h. Due to the U-Net segmentation that provides accurate quantification (Figure 6i), the 3D volume of electrolyte depletion in the R2 sample (32.65 mm^3) is almost four times larger than that in the F3 sample (8.56 mm^3).
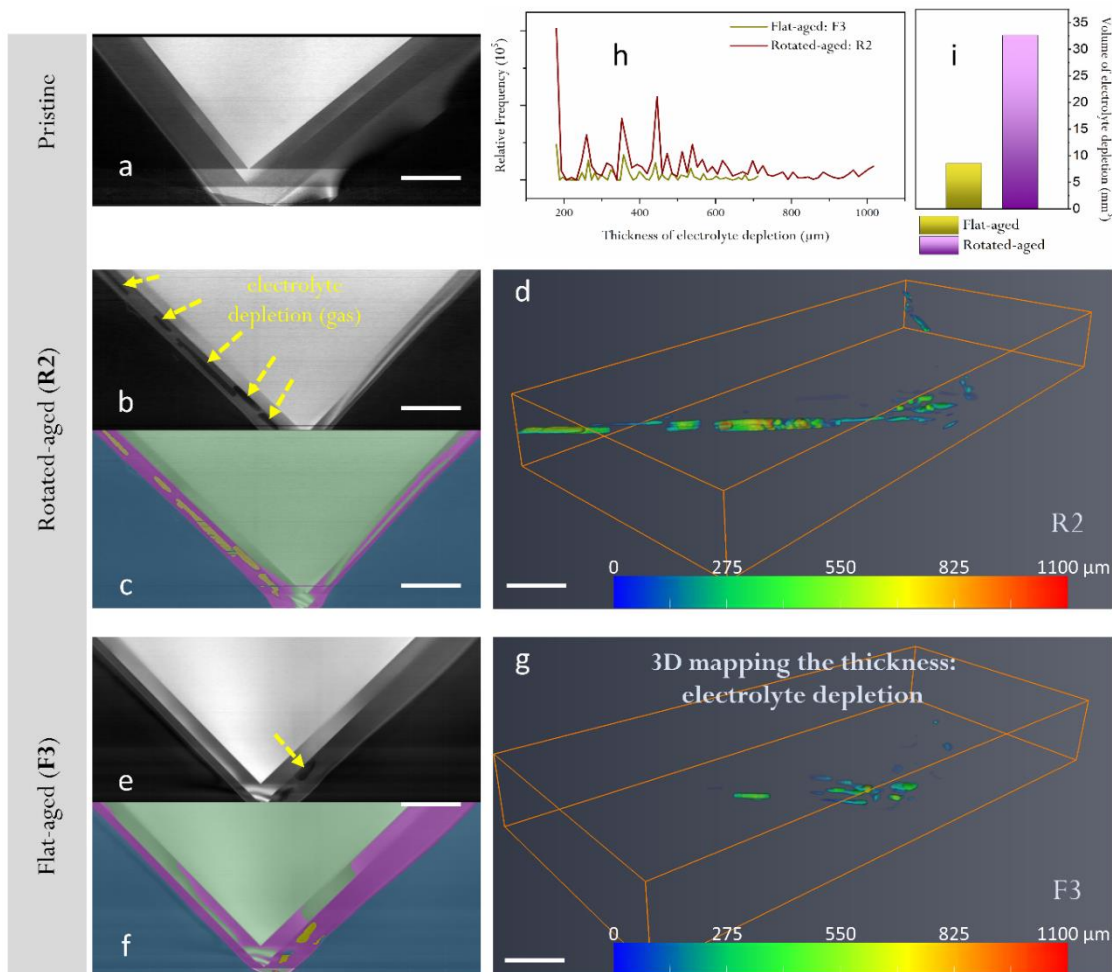

Figure 6. 3D macrostructure of large Li-ion cells at the corner opposite the tabs under the status of (a) pristine, (b–d) rotated-aged, and (e–g) flat-aged. Correspondingly, 2D front views (a, b, and e) are raw tomographic slices (Y-Z plane) selected from the same ROI volumes, and greyscale images are labelled in colours (c & f) after deep learning-assisted segmentation. The pink arrows also highlight the regions of electrolyte depletion. The electrolyte loss (consumption) is rendered in 3D, coupling with their thickness mappings (d & g). The 32 colour bars represent the thickness distribution of electrolyte loss, ranging from 0 to 1100 µm. The quantifications of electrolyte loss for both cases containing (h) the thickness distribution and (i) the measured volumes in 3D. CT results provide

vital evidence that the rotated-aged (R2) sample decomposed more electrolyte (generated more gas products) than the flat-aged (F3) sample. The scale bars are 4 mm for (a–g).

3.5   XRD measurements

In previous work and literature[13], it is presented that the Nissan Leaf cathode contains LMO and LNO. However, since then ICP-OES analysis of dismantled first-generation Nissan Leaf cells from the same battery pack has revealed that the cathode chemistry is LMO and NCA.[39] The results from this experiment confirm that the content ratio of LMO to NCA in the blended cathode is approximately 3:1.

The lattice parameters and weight percentage of each phase present in the cell were refined at each point measured. Figure 7 shows the spatial variation in the lattice parameters of the cathode materials, $LiMn_2O_4$ and NCA, and the graphite c lattice parameter, which is directly related to the interlayer distance by $c/2$, across the cell. The graphite a lattice parameter was fixed at 2.464 Å[51] due to most of the graphite peaks being of low intensity and obscured by the other phases. The plots only cover the area of the cell where both cathode and anode sheets are present; at the edges of the cell, diffraction peaks mainly arise from the aluminium or copper tabs and the laminate pouch cell casing, which contains aluminium and polypropylene. As can be seen in Figure 7, there are significant differences between the spatial variation in the lattice parameters between the two flat-aged cells (F2 & F3) and the rotated-aged cell (R3) that was measured. In the flat-aged cells, there is a front emanating from the top tab-end of the cell, where the $LiMn_2O_4$ and NCA a lattice parameters are larger, spreading towards the bottom of the cell. In these two cells, the NCA c lattice parameter is smaller at the tab-end of the cell but is larger where the front in the change in the NCA a lattice parameter is located. In the rotated-aged cell, the $LiMn_2O_4$ and NCA a lattice parameters are larger in the bottom and right-hand side of the cell and smaller in the top left of the cell whereas the NCA c lattice parameter is larger on the left-hand side of the cell and smaller on the right-hand side of the cell.

Pristine $LiMn_2O_4$, has an a lattice parameter of 8.2261(2) Å,[52] which decreases to 8.03 Å when charged to 4.5 V after going through two phase transitions[53]. With the lattice parameters for $LiMn_2O_4$ ranging from $8.2012(2) \leq a/Å \leq 8.2044(3)$ (see Table 2) the spinel material appears to be partially delithiated but still isostructural to the fully lithiated phase. The change in the lattice parameters of NCA on charging/delithiation is more complex. The a lattice parameter decreases from 2.865 to 2.814 Å on charging to 4.3 V while the c lattice parameter increases from 14.244 Å to 14.469 Å up to 4.1 V before decreasing back to 14.394 Å at 4.3 V.[54] The lattice parameters of other layered oxide materials follow a similar trend.[55,56] Across all the cells, the NCA lattice parameters are in the region of $2.8210(3) \leq a/Å \leq 2.82370(16)$ and $14.4288(12) \leq c/Å \leq 14.4515(20)$, suggesting that the NCA phase remains highly delithiated despite the pouch cell being in a discharged state. It is assumed that changes in the lattice parameters across the cell correlate with variations in Li-content/SoC of the cathode material. In the flat-aged cells, the relithiation of the cathode material stems from the tab-end of the cell and migrates

towards the bottom of the cell, while in the rotated-aged cell the relithiation occurs predominantly from right-to-left. For all cells, the negative (or anode) tab was orientated to the top left of the cell for the measurement, in keeping with the other techniques outlined in the paper. The R3 cell was aged while orientated with the left side of the cell pointing upwards and the right side of the cell pointing downwards so here relithiation is occurring at a faster rate towards the bottom of the cell. The island in the R3 cell where the NCA a lattice parameter is slightly larger is a cross-over point between the tab to the bottom of the cell relithiation direction favoured in the flat-aged cell and the right to left relithiation present in the rest of the rotated-aged cell. On the anode side, there is also an area of slightly increased graphite c lattice parameter towards the tab-end of the flat-aged cells, which is more prominent in the F3 cell. There is also a small area where the graphite c lattice parameter is expanded in the rotated-aged cell in a similar region to the feature in the NCA a lattice parameter.
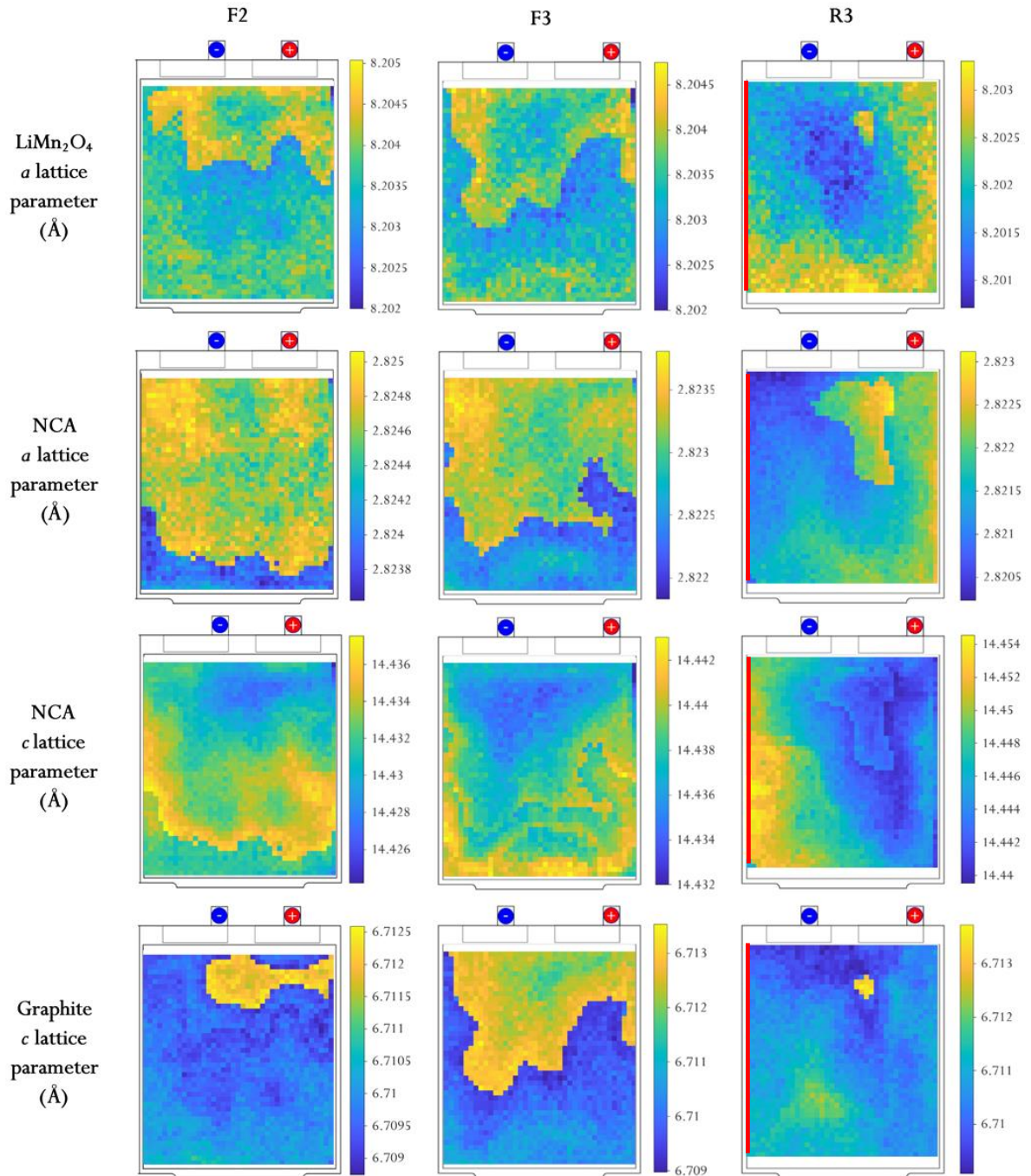
Figure 7. The spatial variation in the LiMn$_2$O$_4$ *a* lattice parameter, NCA *a* and *c* lattice parameters and graphite *c* lattice parameter across the two flat-aged (F2 and F3) and one rotated-aged cell (R3). The maps are overlayed onto schematics of each pouch cell to give the position and the colour bar gives the range of each refined parameter. For rotated cells, the edges oriented upwards are marked with red lines to illustrate the effect of gravity.

Figure 8 shows a probability density estimate of the distribution in the lattice parameters across each map in Figure 7. This plot facilitates a comparison of how the average lattice parameter, or range of lattice parameters, varies from cell to cell. As can be seen from Figure 8, the variation in the lattice parameter across a map does not follow a normal distribution and tends to have several peaks. The probability density distribution generated from each map was fitted with the minimum number of

gaussian functions required to provide a reasonable fit to the distribution. The peak positions within each distribution are summarised in Table 3.
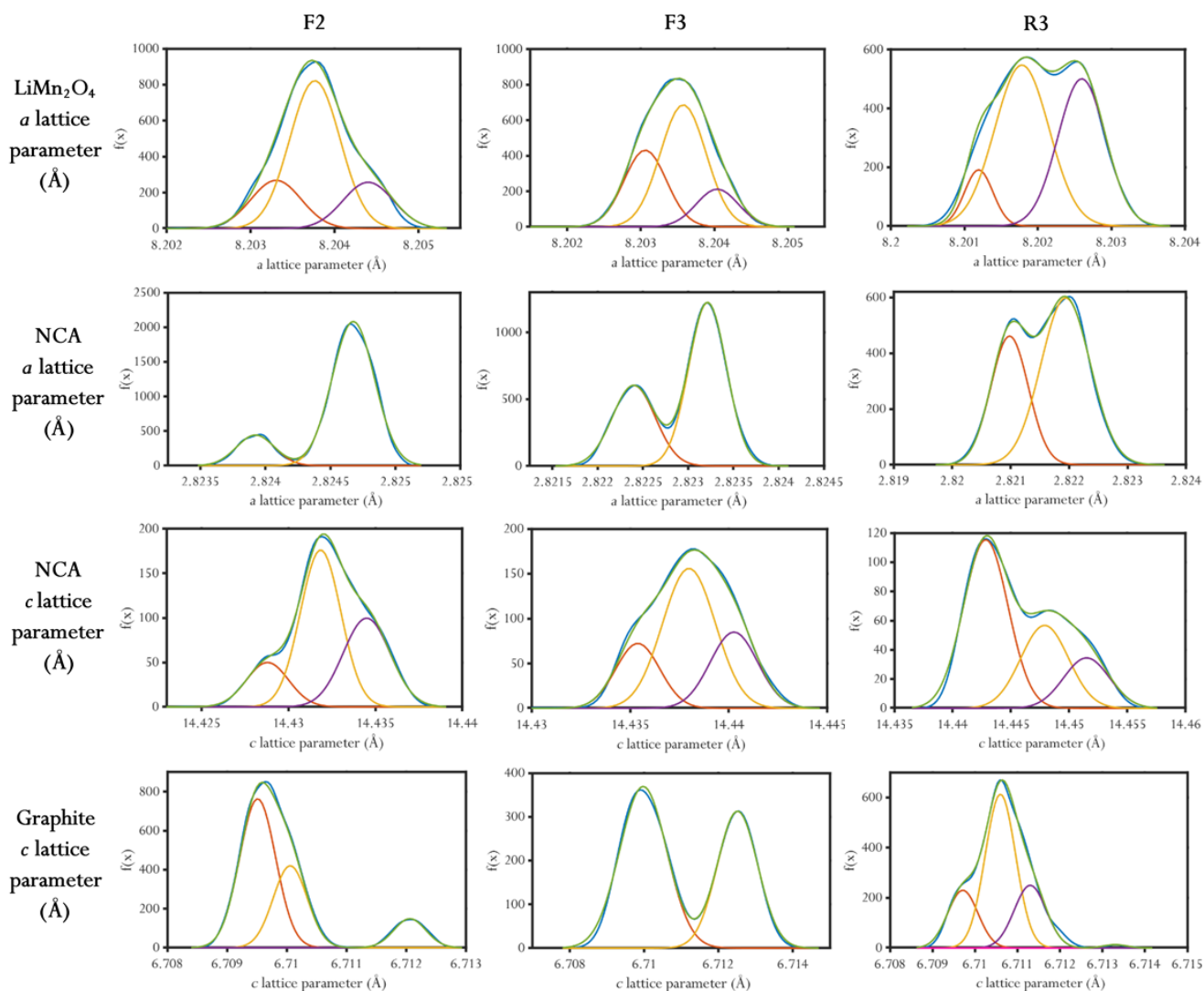

Figure 8. Probability density estimates to visualise the distribution in the LiMn$_2$O$_4$ a lattice parameter, NCA a and c lattice parameters and graphite c lattice parameter across the two flat-aged (F2 and F3) and the rotated-aged cell (R3). Each distribution has been fitted with the minimum number of gaussian peaks to provide a reasonable fit.

Table 3. The position of peaks within the distribution of lattice parameters across each cell

	F2	F3	R3
$LiMn_2O_4$ a lattice parameter (Å)	8.2033(3), 8.2038(3), 8.2044(3)	8.2031(3), 8.2036(3), 8.2040(3)	8.2012(2), 8.2018(4), 8.2026(3)
NCA a lattice parameter (Å)	2.82390(15), 2.82470(16)	2.8224(2), 2.8232(2)	2.8210(3), 2.8219(4)
NCA c lattice parameter (Å)	14.4288(12), 14.4319(12), 14.4345(13)	14.4354(11), 14.4380(13), 14.4403(12)	14.4428(19), 14.4479(21), 14.4515(20)
Graphite c lattice parameter (Å)	6.7095(3), 6.7101(3), 6.7121(3)	6.7100(5), 6.7125(5)	6.7097(4),6.7106(4), 6.7113(4), 6.7133(3)

As can be seen from Table 3, there is a small decrease in the $LiMn_2O_4$ a lattice parameter in the F3 cell compared to the F2 cell but a substantial decrease in the $LiMn_2O_4$ a lattice parameter in the R3 cell. The variation in the NCA lattice parameters is more pronounced between cells; the NCA a lattice parameter decreases from cell F2 to F3 to R3 while the c lattice parameter increases. This implies that the cathode material in the R3 cell is the most delithiated followed by the F3 cell and then the F2 cell cathode material has the highest lithium content. If the increased state of delithiation of the cathode materials in the R3 cell is due to an overall loss in lithium inventory, then it could explain the reduced capacity measured in the R3 cell compared to the F2 and F3 cells (and the capacity of the F3 cell being slightly worse than the F2 cell). From the distribution of the graphite c lattice parameters there seems to be two major phases – both within error of the standard c lattice parameter of graphite (6.711(4) Å) but with one phase centred around c=6.710 Å and the other with a slightly expanded interlayer spacing (c ~ 6.7123 Å). This change is too small to be from the formation of a lithiated graphite phase such as LiC_{30},[57] although the change in lattice parameter could originate from a single layer and be averaged out across the 18 double-sided anode sheets in the cell. The ratio of these two peaks varies from cell to cell with the F3 cell containing the most of this expanded phase and the R3 cell the least, although there is an additional small peak with an even higher c lattice parameter of 6.7133(3) Å. As well as potentially being a small amount of intercalated lithium in some of the graphite, it is possible that in these areas the graphite has become slightly exfoliated. Ex-situ analysis, however, would be required to determine the exact cause of the features.

The variation in the refined weight percentage (wt%) of each phase across a cell is shown in Figure S8. Although there is some fluctuation in the proportion of each phase (e.g. ~4 wt% for $LiMn_2O_4$) across a cell, overall the composition of the cell appears to be quite uniform. The only exception is that the cathode materials, graphite (and copper to some extent) appear to make up a greater proportion of the cell at the top edge of the cell at the expense of the aluminium in all the cells measured. This feature could arise from the manufacturing process rather than through degradation. The spinel (LMO)

comprises the major phase of the blended cathode material, being three times more abundant than the layered (NCA) oxide material.

4.   Discussion

For the first time, this paper presents a case study with multiple modalities to rationalise the understanding of the effect of cell orientation and location in a pack on its inhomogeneity, as well as providing insight into the effectiveness of different techniques for assessing the SoH of cells. This work also provides valuable information regarding state-of-the-art of EV LIBs and acts as a benchmark for future work.

Results presented in thermal imaging, Section 3.2, show that the measured capacity of the flat-aged cells (F2 and F3) is higher compared to the rotated ones (R2 and R3), and the maximal SoH-based capacity difference is 2.8% (Table 1). Such a difference is not so significant and, based on this parameter only, it could be concluded that all four cells in the battery pack aged in a similar way. However, analysis of batteries' in-plane temperature derivative maps and their hot-spot positions during discharging (Video S1 and Figure 3b) gave an insight into the different in-plane ageing for the flat-aged and rotated-aged cells. The temperature derivative map (*dT/dt*) hot-spot moves towards the cell edge that was oriented upwards in the battery pack (for R2 cell to the positive tab and R3 cell to the negative tab side) in the range of 20% - 60% DoD. It is hypothesised that this phenomenon can be explained by the orientation of the cell in the pack causing the area near the edge opposite to the gravity vector, on the upwards side of the cells, to be less wetted by electrolyte compared to the other side battery edge. As a result, during use, the resistance (and ageing) of this part of the cell will increase. Discharging from 60–100% DoD shows that for rotated-aged cells, hot-spot movement is towards the middle of the cells. One of the reasons for this movement is that local DoD, for more aged areas, increases faster during discharging, relative to the less aged areas. After 60% DoD, local current densities (and heat generation) can be higher for less aged areas, leading to the hot-spot movement observed.

The acoustic ultrasonic mapping method can also distinguish between the rotated R and flat F cells and confirms the non-uniform and greater ageing in the rotated cells. These results correlate to the thermal data, which displays the increased temperature under the positive tab, especially in R3, which likely caused the area of low signal attenuation (Figure 4). In R2, there is a low amplitude section that appears in a similar place, directly under the negative tab and spread across to the edge closest to the positive tab, as the points of maximum temperature in the thermal imaging plot (Figure 3). This increased degradation displayed using ultrasonic ToF and thermal data explains why the rotated cells have reduced SoH, albeit (2.8%), and capacity compared to the flat cells.

Since the consumption of electrolyte by the anode (graphite) is well known to be one of the most relevant degradation phenomena,[58] the level of electrolyte depletion could be seen as a health index for evaluating the cells. It is suspected that the higher acoustic attenuation is due to electrolyte depletion in

the aged cells. The middle of the cell is where it is likely most of the electrolyte has been consumed during cycling, and it follows that it is this area where the signal amplitude is lowest. As well as all cells being aged in the middle, the rotated cells also contain larger areas of non-uniform degradation spread away from the middle, relative to the flat cells, explaining the reduced capacity and SoH displayed in Table 1. Due to gravity, the electrolyte in the rotated cells will move to the lower section of the cell leaving the upper section less wetted. The disparity in the amount of electrolyte covering the electrode particles in the cell will have caused increased stress and resistance whilst cycling. This resistance will have likely led to degradation to the internal structure and hence changes to the density and modulus of the material as well as increased non-uniform electrolyte depletion. The change will cause the signal to be dampened and attenuated relative to the Pristine cell. There are no low amplitude areas present in the centre of the Pristine cell because it has not been cycled and hence is not aged.

As well as electrolyte consumption and unwetting, gas is produced inside the cells during cycling. This gas firstly is produced due to the formation of the solid electrolyte interphase (SEI).[59] Then, as the cell is cycled and ages, further reactions with electrolyte and the internal structure of the cell will lead to further evolution.[60] Gas has a far greater acoustic impedance than solid electrode or liquid electrolyte. Therefore, the attenuation of the transmitted ultrasonic signal will be even greater since reflection and scattering at solid-gas interfaces are much more substantial than in solid-solid or solid-liquid interfaces. This gas formation is another reason for the red, low-intensity areas seen in the ultrasound colour maps (Figure 4). The rotated and flat cells are held at the same compression in the pack, meaning the generated gas would not be affected by compression differences between the two orientations. The ultrasound mapping measurements provide very similar information to the thermal imaging regarding the ageing in the cells, but in a faster and easier method, highlighting its usefulness as a technique for determining SoH.

It is well recognised that the high accuracy of electrode alignment between anode and cathode can generate a homogeneous environment including the current distribution and Li movement. However, to date, the investigation of electrode alignment in large-format pouches is limited. Herein, this paper used the corner scan by macro-CT to non-destructively inspect the 3D interior structure that can be correlated with its electrochemical performance and other techniques. Kim *et al.*[61] demonstrated that misaligned cells show a faster capacity fade and lower charge transfer resistance (R_{ct}) than well-aligned cells due to the irreversible loss of Li inventory within coin cells. Interestingly, similar results have been found in the large pouch cells examined here. R2 cell presents a larger electrode misalignment than the F3 cell (Figure 5). It is suspected that the rotated orientation and misaligned layers accelerate its degradation. Misalignment is a problem because it causes a reduction in surface area overlap between the electrode layers, meaning that lithium is left inactive during cycling and in turn causes capacity loss. Indeed, from the electrochemical impedance spectroscopy (EIS) results of our previous study,[13] the R2 (misaligned cell) has a lower value of R_{ct} than F3 (aligned cell) in all SoCs. Furthermore, the quantitative analysis

for acoustic mapping (Figure S3) suggests that the fraction of the most degraded region (gas region) in the R2 cell (24.3 %) is almost double that in the F3 cell (12.6 %), as depicted in Table 2. Also, the capacity retention at EOL for the R2 cell is 27.7 Ah, whilst it is 28.2 Ah for the F3 cell (Figure 2b).2D lateral inhomogeneous ageing in all battery cells was captured and identified by infrared thermography (Figure 3), ultrasonic mapping (Figure 4), and HELM (Figures 7 & 8) techniques. The CT technique (Figures 5 & 6) can further interrogate the localised inhomogeneity in 3D, and gain insights into the specific failure mechanisms caused by different orientations. CT confirmed the suspected results seen in the other techniques; for the rotated cells, the electrolyte depletion can be visualised in the bottom right of R2 (Figure 6). Whilst the CT scans only image the corner of the cell, the electrolyte depletion and gas formation seen likely spreads into centre of the cell, especially for the rotated cells. The acoustic mapping appears to confirm this gas generation/electrolyte reactions in the centre of the cell because of the areas of high signal attenuation. These results emphasise the importance of the correlated techniques in forensic analysis of aged cells, allowing inferences from one technique to be confirmed with additional characterisation. The findings are also supported by measuring the overall resistance R in the previous work of Milojevic *et al.*[13]

For the dewetted regions, due to either electrolyte dry-out or decomposition, where there is insufficient solvent to solvate Li-ions, an increased R is measured. Thus, it was expected that inhomogeneity negatively affects battery performance. The nature of rotated orientation generates an undesired electrolyte gradient. The less wetted particles fade faster and lead to the thermal gradient which has been detected by thermal imaging (Figure 3). The inhomogeneous electrolyte gradient could result in a non-uniform SEI film at the very beginning of cell life which will affect the safety, durability and rate capability[62]. This inhomogeneity is likely to be accelerated as the cell ages. Hence, it is speculated that planar electrolyte diffusion will effectively alleviate the planar heterogeneity in electrolyte distribution and electrochemical reaction. It is important to note that whilst the electrolyte gradient influences degradation, and the location of degradation, it is not the only contributing factor. If degradation was just down to electrolyte gradient, then one side of the rotated cell would be completely degraded and the other would not. Instead, the electrolyte gradient exacerbates the degradation process.

Suppressing inhomogeneous electrolyte depletion such as that observed in this study may require more attention from EV pack designers and manufacturers as they move towards using larger cells to achieve higher energy densities. It is also anticipated that the characterisation of electrode particles at 'particle level' in flat and rotated cells will provide further evidence of inhomogeneity. The correlation of X-ray imaging with high flux techniques, such as Hierarchical Phase-Contrast Tomography (HiP-CT) at ERSF,[63] could open up a new opportunity to bridge the common scale issues and advance battery development.

HELM showed a gradient in the SoC, or the extent of relithiation on discharge across the cell. In the flat-aged cells, relithiation was more advanced in the cathode materials towards the tab-end of the cell compared to the bottom edge and corners of the cell. This correlated with the direction of travel of the hot-spots in the IR thermal imaging with the location of the hot-spots migrating from the tab towards the centre of the cell on discharge. The rotated-aged cells dT/dt_{Max} hot-spots had an additional significant movement towards the side of the cell that oriented towards the upper edge, opposite to the gravity vector, after the initial movement away from the tabs. This movement is in keeping with the SoC gradient in the R3 cell, which had an area of more advanced relithiation to the left of the positive tab and the bottom of the cell. It is known that thermal inhomogeneities in cells can create a variation in local cell impedance and current density[64,65] and in turn cause differences in the SoC across a cell.[66] Higher current densities at the tabs of pouch cells have also been experimentally confirmed[67] and in an in-situ synchrotron X-ray diffraction experiment on a pouch cell the area under the positive tab was found to be of a higher SoC compared to the rest of the cell.[5] In a separate HELM study on a single-phase NMC622 pouch cell, Yu *et al.* found that the edges and corners were of a lower SoC than the middle of cell.[68] Their results compare to similar observations in the ultrasound maps of this paper, where the greatest ageing was seen in the centre of the cell. The changing orientation of the cell adds an additional factor to determining gradients in the SoC. The rotated cell may aid Li-diffusion and cause more rapid relithiation in the electrolyte-rich part of the cell compared to the de-wetted region. The fact the relatively cheap thermal imaging measurements can detect the SoC and degradation gradient displayed in expensive synchrotron experimental results is vital for the development of end-of-life cell testing on a large scale.

An interesting observation is the significantly higher SoC and consequently the greater state of delithiation of the NCA cathode material compared to $LiMn_2O_4$ (LMO). Using NCA in combination with LMO is thought to reduce the amount of Mn-dissolution from the spinel phase and mechanical stress in LMO during Li insertion/desertion, improving capacity retention.[69,70] However, when a blend of cathode materials is used, a compromise must be made on the voltage range. LMO is most electrochemically active above 3.9 V and finishes charging at 4.3 V, while NCA is more electrochemically active below 3.9 V and starts to experience accelerated fatigue above 4.05 V (vs. Li) with increased microcracking and surface modifications, such as rock-salt or spinel phase formation.[71] This will slow the rate of Li-diffusion into the NCA particles and lead to a higher charge transfer resistance. It is important to note that while previous work has seen interesting degradation phenomena linked to fatigue of cathode material at the top of charge,[5,72] it is also known that there are kinetic limitations to the re-insertion of Li at the bottom of charge,[73] and so exploring the spatial variation of this via HELM at bottom of charge is indicative of kinetic degradation phenomena. Moreover, while elevated temperatures will enhance the rate of degradation of LMO and NCA, NCA is more severely affected. A prior *in-situ* XRD study on a cathode material consisting of a blend of LMO, NCA and

NMC found that after cycling at 40°C the NCA phase became electrochemically inactive with little changes in the lattice parameters on cycling and no evidence of Li insertion/deinsertion[74]. In the present work on the LMO/NCA cathode blend, although there was some evidence of lithium loss from the LMO through a reduction in the *a* lattice parameter, changes in the lattice parameters of the NCA phase corresponding to delithiation were much more marked. A loss in the lithium inventory of the cell through SEI formation can cause a shift in the anode and cathode potentials resulting in an overcharging of the cathode material.[72] As LMO is more stable at higher voltages than NCA, any overcharging is likely to degrade NCA to a much greater extent than the LMO. This degradation may impede the relithiation of the NCA. In the HELM study, the average lattice parameters are correlated with the capacities of the cells with the R3 cell having the lowest capacity and lattice parameters corresponding to the cathode materials being the most delithiated compared to the F2 and F3 cells. This suggests a lower Li-inventory is present in the R3 cell as at full discharge there is less Li present to relithiate the cathode material. From the ultrasound mapping and CT measurements, the rotated cells had a higher degree of electrolyte consumption and gas generation than the flat-aged cells, showing a more advanced level of degradation. Since gas generation can be caused by SEI formation, thus it could explain the lower Li-inventory in the rotated-aged cell.

5.   Conclusion

This paper has outlined the success of using non-destructive techniques to estimate the SoH of large-size EV pouch cells. The work has shown the importance of the orientation and location of cells inside a battery pack when deciding the next use for cells at their supposed EoL. Four non-destructive techniques: infrared thermography, ultrasonic acoustic mapping, X-ray computed tomography, and synchrotron powder X-ray diffraction were used in the study. It was shown that rotated cells displayed substantially different and more severe ageing patterns after their first-life usage, compared to the flat cells, after the same period of use. In contrast, a pristine cell was seen to be relatively uniform and show no discernible degradation within the cell structure. Each technique, recorded at different times, all correlated together to confirm similar results. The electrolyte gradient within the rotated cells contributed to the differing degradation observed. In the flat cells, the electrolyte was wetted uniformly meaning that, during cycling, both electrodes had an equal covering of electrolyte and therefore no disparity in resistance when ions were transferred. However, the rotated cells contain less liquid electrolyte on one electrode than the other due to gravity. As the battery pack is used during EV life, the electrolyte is consumed due to ageing mechanisms leading to increased charge transfer and SEI layer resistance. This resistance is greater for the rotated cells as one electrode will become drier sooner, leading to increased stress on the rotated cells and hence enhanced degradation. In an EV application, such electrolyte depletion cannot be ignored. The results give clear evidence to manufacturers about how to mitigate heterogeneous degradation by careful consideration of orientation effects during battery pack design.

The CT results demonstrate that deep learning-assisted segmentation tools can play a valuable role in X-ray imaging analysis. The next steps are to implement these techniques on a far greater scale with many more cells. The more expensive but more detailed X-ray techniques have been shown to confirm what was suspected by the low-cost, non-invasive IR thermography and ultrasound measurements. Therefore, there is evidence that these low-cost non-destructive techniques alone can give accurate degradation information, allowing for a rapid decision on the cells EoL to be made, whether that be recycling, repurpose or reuse in a second-life application such as stationary storage.

Author contributions

Conflicts of interest

There are no conflicts of interest to declare

Acknowledgements

References

1. Hosseinzadeh, E. *et al.* A systematic approach for electrochemical-thermal modelling of a large format lithium-ion battery for electric vehicle application. *J. Power Sources* **382**, 77–94 (2018).
2. Mei, W., Chen, H., Sun, J. & Wang, Q. The effect of electrode design parameters on battery performance and optimization of electrode thickness based on the electrochemical-thermal coupling model. *Sustain. Energy Fuels* **3**, 148–165 (2019).
3. Goutam, S. *et al.* Three-dimensional electro-thermal model of li-ion pouch cell: Analysis and comparison of cell design factors and model assumptions. *Appl. Therm. Eng.* **126**, 796–808 (2017).
4. Yi, J., Kim, U. S., Shin, C. B., Han, T. & Park, S. Three-Dimensional Thermal Modeling of a Lithium-Ion Battery Considering the Combined Effects of the Electrical and Thermal Contact Resistances between Current Collecting Tab and Lead Wire. *J. Electrochem. Soc.* **160**, A437–A443 (2013).
5. Leach, A. S. *et al.* Spatially Resolved Operando Synchrotron-Based X-Ray Diffraction Measurements of Ni-Rich Cathodes for Li-Ion Batteries. *Front. Chem. Eng.* **3**, 1–9 (2022).
6. Kim, G.-H., Smith, K., Lee, K.-J., Santhanagopalan, S. & Pesaran, A. Multi-Domain Modeling of Lithium-Ion Batteries Encompassing Multi-Physics in Varied Length Scales. *J. Electrochem. Soc.* **158**, A955 (2011).
7. Veth, C., Dragicevic, D., Pfister, R., Arakkan, S. & Merten, C. 3D Electro-Thermal Model Approach for the Prediction of Internal State Values in Large-Format Lithium Ion Cells and Its Validation. *J. Electrochem. Soc.* **161**, A1943–A1952 (2014).
8. Bandhauer, T. M., Garimella, S. & Fuller, T. F. A Critical Review of Thermal Issues in Lithium-Ion Batteries. *J. Electrochem. Soc.* **158**, R1 (2011).
9. Waldmann, T. *et al.* Influence of Cell Design on Temperatures and Temperature Gradients in Lithium-Ion Cells: An In Operando Study. *J. Electrochem. Soc.* **162**, A921–A927 (2015).
10. Veth, C., Dragicevic, D. & Merten, C. Thermal characterizations of a large-format lithium ion cell focused on high current discharges. *J. Power Sources* **267**, 760–769 (2014).
11. Attidekou, P. S. *et al.* Methodologies for Large-Size Pouch Lithium-Ion Batteries End-of-Life Gateway Detection in the Second-Life Application. *J. Electrochem. Soc.* **167**, 160534 (2020).
12. Robinson, J. B. *et al.* Detection of internal defects in lithium-ion batteries using lock-in thermography. *ECS Electrochem. Lett.* **4**, A106–A109 (2015).
13. Milojevic, Z. *et al.* Influence of orientation on ageing of large-size pouch lithium-ion batteries during electric vehicle life. *J. Power Sources* **506**, (2021).
14. Majasan, J. O. *et al.* Recent advances in acoustic diagnostics for electrochemical power systems. *JPhys Energy* vol. 3 (2021).
15. Popp, H., Koller, M., Jahn, M. & Bergmann, A. Mechanical methods for state determination of Lithium-Ion secondary batteries: A review. *Journal of Energy Storage* vol. 32 (2020).
16. Robinson, J. B. *et al.* Spatially resolved ultrasound diagnostics of Li-ion battery electrodes. *Phys. Chem. Chem. Phys.* **21**, 6354–6361 (2019).
17. Robinson, J. B. *et al.* Identifying Defects in Li-Ion Cells Using Ultrasound Acoustic Measurements. *J. Electrochem. Soc.* **167**, 120530 (2020).
18. Deng, Z. *et al.* Ultrasonic Scanning to Observe Wetting and "Unwetting" in Li-Ion Pouch Cells. *Joule* **4**, 2017–2029 (2020).
19. Gauthier, R. *et al.* How do Depth of Discharge, C-rate and Calendar Age Affect Capacity Retention, Impedance Growth, the Electrodes, and the Electrolyte in Li-Ion Cells? *J. Electrochem. Soc.* (2022) doi:10.1149/1945-7111/ac4b82.
20. Xie, Y. *et al.* Inhomogeneous degradation induced by lithium plating in a large-format lithium-ion

battery. *J. Power Sources* **542**, 231753 (2022).

21. Heenan, T. M. M., Tan, C., Hack, J., Brett, D. J. L. & Shearing, P. R. Developments in X-ray tomography characterization for electrochemical devices. *Materials Today* vol. 31 69–85 (2019).

22. Lu, X. *et al.* 3D microstructure design of lithium-ion battery electrodes assisted by X-ray nano-computed tomography and modelling. *Nat. Commun.* **11**, 1–13 (2020).

23. Taiwo, O. O. *et al.* Microstructural degradation of silicon electrodes during lithiation observed via operando X-ray tomographic imaging. *J. Power Sources* **342**, 904–912 (2017).

24. Zwanenburg, E. A., Williams, M. A. & Warnett, J. M. Review of high-speed imaging with lab-based x-ray computed tomography. *Meas. Sci. Technol.* **33**, (2022).

25. Withers, P. J. *et al.* X-ray computed tomography. *Nat. Rev. Methods Prim.* **1**, (2021).

26. Kok, M. D. R. *et al.* Virtual unrolling of spirally-wound lithium-ion cells for correlative degradation studies and predictive fault detection. *Sustain. Energy Fuels* **3**, 2972–2976 (2019).

27. Finegan, D. P. *et al.* In-operando high-speed tomography of lithium-ion batteries during thermal runaway. *Nat. Commun.* **6**, 1–10 (2015).

28. Robinson, J. B. *et al.* Non-uniform temperature distribution in Li-ion batteries during discharge - A combined thermal imaging, X-ray micro-tomography and electrochemical impedance approach. *J. Power Sources* **252**, 51–57 (2014).

29. Jnawali, A. *et al.* Motion-enhancement assisted digital image correlation of lithium-ion batteries during lithiation. *J. Power Sources* **527**, 231150 (2022).

30. Bond, T., Gauthier, R., Eldesoky, A., Harlow, J. & Dahn, J. R. In Situ Imaging of Electrode Thickness Growth and Electrolyte Depletion in Single-Crystal vs. Polycrystalline LiNixMnyCozO2/Graphite Pouch Cells using Multi-Scale Computed Tomography. *J. Electrochem. Soc.* (2022) doi:10.1149/1945-7111/ac4b83.

31. Du, W. *et al.* In-situ X-ray tomographic imaging study of gas and structural evolution in a commercial Li-ion pouch cell. *J. Power Sources* **520**, 230818 (2022).

32. Shateri, N. *et al.* Investigation of the Effect of Temperature on Lithium-Sulfur Cell Cycle Life Performance Using System Identification and X-Ray Tomography. *Batter. Supercaps* **202200035**, (2022).

33. Harper, G. *et al.* Recycling lithium-ion batteries from electric vehicles. *Nature* **575**, 75–86 (2019).

34. Hu, X. *et al.* Advanced Fault Diagnosis for Lithium-Ion Battery Systems: A Review of Fault Mechanisms, Fault Features, and Diagnosis Procedures. *IEEE Ind. Electron. Mag.* **14**, 65–91 (2020).

35. Llewellyn, A. V., Matruglio, A., Brett, D. J. L., Jervis, R. & Shearing, P. R. Using in-situ laboratory and synchrotron-based x-ray diffraction for lithium-ion batteries characterization: A review on recent developments. *Condens. Matter* **5**, 1–28 (2020).

36. Xu, C. *et al.* Bulk fatigue induced by surface reconstruction in layered Ni-rich cathodes for Li-ion batteries. *Nat. Mater.* **20**, (2021).

37. Mattei, G. S. *et al.* High-Energy Lateral Mapping (HELM) Studies of Inhomogeneity and Failure Mechanisms in NMC622/Li Pouch Cells. *Chem. Mater.* **33**, 2378–2386 (2021).

38. Paul, P. P. *et al.* Using in Situ High-Energy X-ray Diffraction to Quantify Electrode Behavior of Li-Ion Batteries from Extreme Fast Charging. *ACS Appl. Energy Mater.* **4**, 11590–11598 (2021).

39. Gastol, D. *et al.* Reclaimed and Up-Cycled Cathodes for Lithium-Ion Batteries. *Glob. Challenges* **2200046**, 2200046 (2022).

40. Owen, R. E. *et al.* Operando Ultrasonic Monitoring of Lithium-Ion Battery Temperature and Behaviour at Different Cycling Rates and under Drive Cycle Conditions. *J. Electrochem. Soc.* **169**, 040563 (2022).

41. Schneider, C. A., Rasband, W. S. & Eliceiri, K. W. NIH Image to ImageJ: 25 years of image analysis. *Nat. Methods* **9**, 671–675 (2012).

42. Otsu, N. *et al.* Otsu_1979_otsu_method. *IEEE Trans. Syst. Man. Cybern.* **C**, 62–66 (1979).

43. Kamarainen, J. Gabor Features in Image Analysis. 12–13 (2012).

44. Wang, R. *et al.* Medical image segmentation using deep learning: A survey. *IET Image Process.* **16**, 1243–1267 (2022).

45. Drakopoulos, M. *et al.* I12: The Joint Engineering, Environment and Processing (JEEP) beamline at Diamond Light Source. *J. Synchrotron Radiat.* **22**, 828–838 (2015).

46. Filik, J. *et al.* Processing two-dimensional X-ray diffraction and small-angle scattering data in DAWN 2. *J. Appl. Crystallogr.* **50**, 959–966 (2017).

47. Evans, J. S. O. Advanced input files & parametric quantitative analysis using topas. *Mater. Sci. Forum* **651**, 1–9 (2010).

48. Coelho, A. A. TOPAS and TOPAS-Academic: An optimization program integrating computer algebra and crystallographic objects written in C++: An. *J. Appl. Crystallogr.* **51**, 210–218 (2018).

49. Otte, H. M. Lattice parameter determinations with an X-ray spectrogoniometer by the debye-scherrer method and the effect of specimen condition. *J. Appl. Phys.* **32**, 1536–1546 (1961).

50.   Kovachev, G. *et al.* Analytical dissection of an automotive Li-ion pouch cell. *Batteries* **5**, (2019).

51.   Trucano, P. & Chen, R. Structure of graphite by neutron diffraction. *Nature* **258**, 136–137 (1975).

52.   Liu, J. *et al.* Unified View of the Local Cation-Ordered State in Inverse Spinel Oxides. *Inorg. Chem.* **58**, 14389–14402 (2019).

53.   Sottmann, J., Pralong, V., Barrier, N. & Martin, C. An electrochemical cell for operando bench-top X-ray diffraction. *J. Appl. Crystallogr.* **52**, 485–490 (2019).

54.   Zhang, N. *et al.* In situ X-ray diffraction and thermal analysis of LiNi0.8Co0.15Al0.05O2 synthesized via co-precipitation method. *J. Energy Chem.* **27**, 1655–1660 (2018).

55.   Märker, K., Reeves, P. J., Xu, C., Griffith, K. J. & Grey, C. P. Evolution of Structure and Lithium Dynamics in LiNi0.8Mn0.1Co0.1O2 (NMC811) Cathodes during Electrochemical Cycling. *Chem. Mater.* **31**, 2545–2554 (2019).

56.   Weber, R., Fell, C. R., Dahn, J. R. & Hy, S. Operando X-ray Diffraction Study of Polycrystalline and Single-Crystal Li x Ni 0.5 Mn 0.3 Co 0.2 O 2 . *J. Electrochem. Soc.* **164**, A2992–A2999 (2017).

57.   Missyul, A., Bolshakov, I. & Shpanchenko, R. XRD study of phase transformations in lithiated graphite anodes by Rietveld method. *Powder Diffr.* **32**, S56–S62 (2017).

58.   Liu, X. *et al.* In situ observation of thermal-driven degradation and safety concerns of lithiated graphite anode. *Nat. Commun.* **12**, (2021).

59.   Leißing, M. *et al.* The Impact of the C-Rate on Gassing During Formation of NMC622 II Graphite Lithium-Ion Battery Cells. *Batter. Supercaps* **4**, 1344–1350 (2021).

60.   Schiele, A. *et al.* Silicon nanoparticles with a polymer-derived carbon shell for improved lithium-ion batteries: Investigation into volume expansion, gas evolution, and particle fracture. *ACS Omega* **3**, 16706–16713 (2018).

61.   Kim, N. *et al.* Electrode Alignment: Ignored but Important Design Parameter in Assembling Coin-Type Full Lithium-Ion Cells. *J. Electrochem. Soc.* **169**, 023502 (2022).

62.   Zhang, Z. *et al.* Operando Electrochemical Atomic Force Microscopy of Solid-Electrolyte Interphase Formation on Graphite Anodes: The Evolution of SEI Morphology and Mechanical Properties. *ACS Appl. Mater. Interfaces* **12**, 35132–35141 (2020).

63.   Walsh, C. L. *et al.* Imaging intact human organs with local resolution of cellular structures using hierarchical phase-contrast tomography. *Nat. Methods* **18**, 1532–1541 (2021).

64.   Mei, W., Liang, C., Sun, J. & Wang, Q. Three-dimensional layered electrochemical-thermal model for a lithium-ion pouch cell. *Int. J. Energy Res.* **44**, 8919–8935 (2020).

65.   Fear, C. *et al.* Mechanistic underpinnings of thermal gradient induced inhomogeneity in lithium plating. *Energy Storage Mater.* **35**, 500–511 (2021).

66.   Fleckenstein, M., Bohlen, O., Roscher, M. A. & Bäker, B. Current density and state of charge inhomogeneities in Li-ion battery cells with LiFePO4 as cathode material due to temperature gradients. *J. Power Sources* **196**, 4769–4778 (2011).

67.   Bason, M. G. *et al.* Non-invasive current density imaging of lithium-ion batteries. *J. Power Sources* **533**, (2022).

68.   Yu, X. *et al.* Simultaneous Operando Measurements of the Local Temperature, State of Charge, and Strain inside a Commercial Lithium-Ion Battery Pouch Cell. *J. Electrochem. Soc.* **165**, A1578–A1585 (2018).

69.   Myung, S. T., Cho, M. H., Hong, H. T., Kang, T. H. & Kim, C. S. Electrochemical evaluation of mixed oxide electrode for Li-ion secondary batteries: Li1.1Mn1.9O4 and LiNi 0.8Co0.15Al0.05O2. *J. Power Sources* **146**, 222–225 (2005).

70.   Dai, Y., Cai, L. & White, R. E. Simulation and analysis of stress in a Li-ion battery with a blended LiMn2O4 and LiNi0.8Co0.15Al 0.05O2 cathode. *J. Power Sources* **247**, 365–376 (2014).

71.   Lang, M. *et al.* Post mortem analysis of fatigue mechanisms in LiNi0.8Co0.15Al0.05O2 – LiNi0.5Co0.2Mn0.3O2 – LiMn2O4/graphite lithium ion batteries. *J. Power Sources* **326**, 397–409 (2016).

72.   Dose, W. M., Xu, C., Grey, C. P. & De Volder, M. F. L. Effect of Anode Slippage on Cathode Cutoff Potential and Degradation Mechanisms in Ni-Rich Li-Ion Batteries. *Cell Reports Phys. Sci.* **1**, 100253 (2020).

73.   Zhou, H., Xin, F., Pei, B. & Whittingham, M. S. What Limits the Capacity of Layered Oxide Cathodes in Lithium Batteries? *ACS Energy Lett.* **4**, 1902–1906 (2019).

74.   Darma, M. S. D. *et al.* The influence of cycling temperature and cycling rate on the phase specific degradation of a positive electrode in lithium ion batteries: A post mortem analysis. *J. Power Sources* **327**, 714–725 (2016).